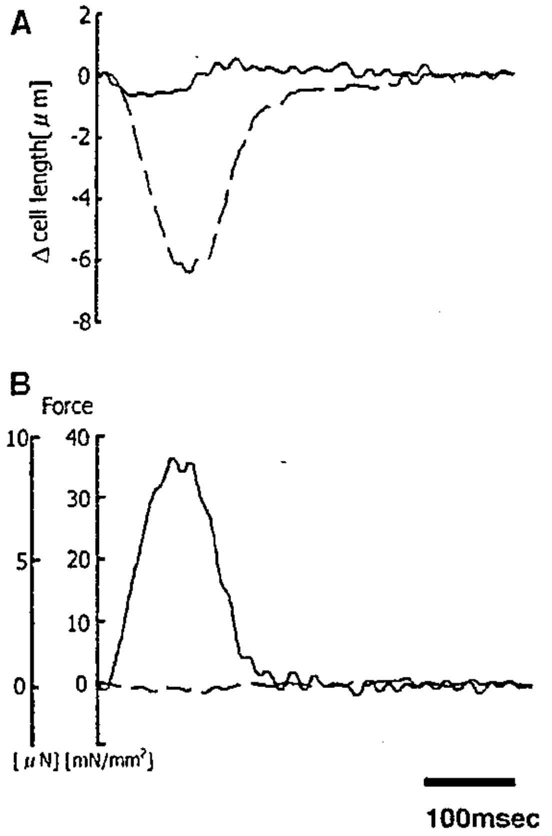

Fig. 3. Cell length and force during isometric and unloaded shortening contractions in the same myocyte. *A*: cell length during isometric (solid line) and unloaded shortening (dashed line) contractions. Length change during the isometric contraction was <0.5 μm. *B*: developed force during the isometric (solid line) and unloaded shortening (dashed line) contractions shown in *A*. During unloaded shortening, the force was zero. In this cell, cross-sectional area was 749 μm^2.

data. The achieved physiological work calculated thus determined in 20 cells was 828 ± 123 J/m^3.

We changed load and obtained a series of force-length loops. The curve connecting the top left corners of these loops was convex upward, analogous to the end-systolic pressure-volume relation of the rodent ventricle (Fig. 4) (12). Applying linear regression to these points yielded a slope of 1,260 ± 108 nN/μm (n = 17 cells).

By stretching the cells before the contraction, we could observe the effect of increasing preload. As shown in Fig. 5, not only the isometric force (Fig. 5*A*) and unloaded shortening length (data not shown) but also the external work (Fig. 5*B*) increased depending on the preload. Because muscle length and force at baseline varied considerably, we could not achieve statistical analysis of this findings, but similar preload dependence was found in 10 cells.

Sarcomere length. We measured sarcomere length and compared it with simultaneously recorded cell length. We confirmed that cell length always changed in parallel with sarcomere length under resting conditions as well as during contraction against low load (Fig. 6*A*). In 12 cells in which sarcomere length signals of good quality were obtained, similar observations were made. Although it was difficult to determine sarcomere length during isometric conditions due to blurring of the sarcomere pattern, we could record it in eight cells. Although

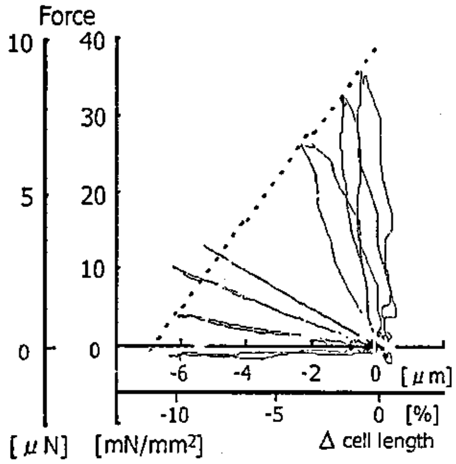

Fig. 4. Force-length loop of a single cardiomyocyte under various loading conditions. Data were obtained during adaptive control for isometric and unloaded shortening as well as simulated ejection. The y-axis shows force (raw data) and force per cross-sectional area (in this cell, cross-sectional area was 749 μm^2). Linear regression was applied to the top left corner points of the loops. The slope of the regression line was 1,730 nN/μm. External work produced by the ejecting contraction was 1,139 J/m^3.

small compared with sarcomere shortening during uncontrolled contraction under unloaded conditions (Fig. 6*B*, solid line), we observed internal shortening of sarcomeres (Fig. 6*B*, dashed line) of the same magnitude (≈0.1 μm) in 8 cells.

DISCUSSION

Single cell mechanics by the carbon fiber technique. In this study, we studied the mechanics of single rat cardiomyocytes over a wide range of loading conditions including isometric, unloaded, and physiological loading conditions. To our knowl-

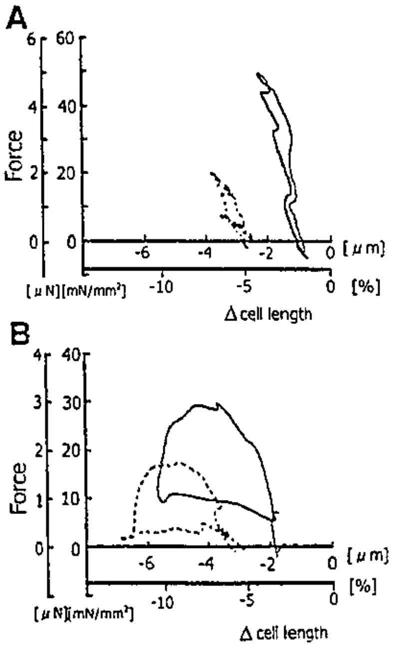

Fig. 5. Preload dependence of contractile function *A*: isometric contractions under two different (solid line 1.78 μm; dashed line 1.71 μm) preloads. *B*: ejecting contractions under two different preloads showing the preload dependence of external work. The y-axis shows force (raw data) and force per cross-sectional area (in this cell, cross-sectional area was 323 μm^2).

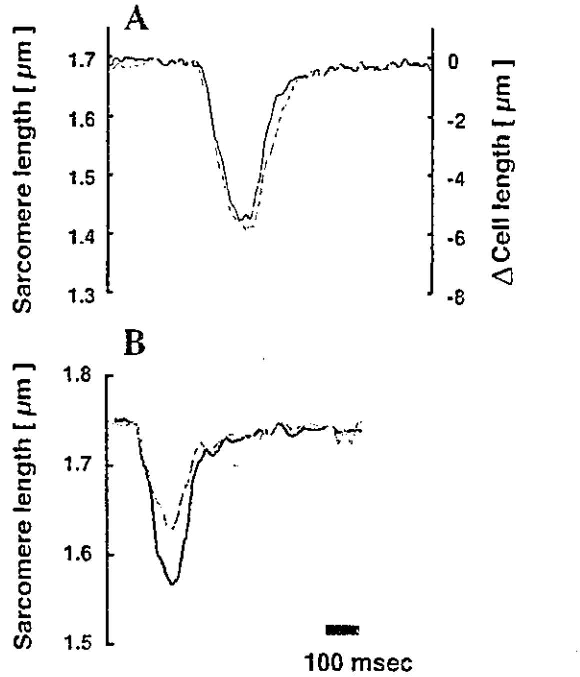

Fig. 6. Relationship between cell length and sarcomere length. *A*: simultaneous recording of cell length (solid line) and sarcomere length (dashed line) during contraction under unloaded conditions. *B*: sarcomere length during isometric contraction (dashed line) and under unloaded conditions (solid line) recorded in the same cell.

edge, this is the first time that physiological force-length loops have been reported in isolated myocytes. Because of its important role in relating subcellular molecular events to ventricular dynamics, many researchers have studied single cell mechanics of cardiomyocytes using various methods (11). Compared with other methodologies, the carbon fiber technique is superior in two aspects. First, it is relatively simple and does not require technical expertise. Second, attachment of carbon fibers results in minimal damage to the sarcolemma (11). With the use of carbon fibers (26), the overall success rate for establishing firm attachment to myocytes was over 80% in this series of experiments, and myocytes remained stable for 10 min of contractions by electric stimulation. This excellent stability enabled us to study myocyte mechanics under various loading conditions as well as under inotropic interventions in the same myocyte, which, in certain cases, was helpful in avoiding cell-to-cell variations. In addition, we obtained a peak isometric force of 5.72 μN in this study. This is in the highest range of twitch force reported so far [Ref. 3 and review by Bluhm et al. (2)] and is ≈75% of the maximally activated force (7.5 μN) (10) obtained in a single skinned rat cardiomyocyte, supporting its usefulness.

Physiological significance. In rat trabeculae preparations, Janssen and de Tombe (14) reported an isometric twitch force of 45 mN/mm^2 for muscle isometric twitches and 88.5 mN/mm^2 for sarcomere isometric twitches. In a left ventricular papillary muscle preparation, isometric force was ~6 g/mm^2 (≈60 mN/mm^2) (5). The isometric force obtained in this study (41.6 ± 5.6 mN/mm^2) was somewhat lower but close to these values. For shortening velocity, we obtained 106 ± 8.9 μm/s, which is equivalent to 1.58 lengths/s (37°C). In rat trabeculae, predominantly containing the V$_1$ myosin isoform, an unloaded shortening velocity of 2.3 lengths/s (30°C) has been reported (20). On the other hand, Josephson et al. (15) measured the maximal shortening velocity of euthyroid rat ventricular myocytes at 29°C and reported a value of 1.17 lengths/s. Again, our results are close to these values, suggesting that carbon fiber attachment does not create extra load if its movement is properly controlled as in this study. However, the key feature required for single cell mechanics is how accurately it can reproduce and describe the behavior of the cell in the body. In response to change in afterload, we obtained a series of force-length loops. The top left corners of these loops distributed along a straight line, analogous to the end-systolic pressure-volume relation of the ventricle (Fig. 4). Furthermore, when inotropic intervention was applied to a single myocyte by adding isoproterenol (2 μM) to the medium, the slope of this line increased in a similar manner with the ventricular end-systolic pressure-volume relation (Fig. 7, *A* and *B*). Preload dependence was also confirmed (Fig. 5). Finally, using digital control, we could obtain physiological force-length loops of a single cardiomyocyte (Fig. 4) resembling those reported in experimental (13) and simulation studies (21, 22). The average work output per unit volume calculated from the stress-relative shortening area was 828 ± 123 J/m^3. If we assume the density of cardiac muscle to be ~1g/cm^3, 1 g of the rat ventricle (cm^3) would generate 0.83 mJ. This value is ~13% of the external work done by a rat ventricle ejecting 500 μl of blood while generating ~100 mmHg. The cause of this discrepancy is not clear, but the lack of sympathetic stimulation to the isolated myocyte could be one of the possibilities.

Adaptive control of cell length and force. With the real-time analog control system we used in previous studies (25, 26), it

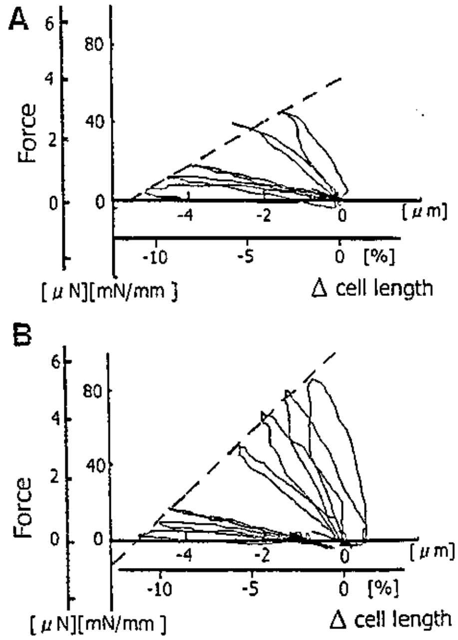

Fig. 7. Force-length relation of a single cardiomyocyte before (*A*) and after (*B*) the addition of isoproterenol (2 μM) to the medium. Isometric force increased from 44 to 85 mN/mm^2, and the slope of the regression line increased from 11 to 19 mN·mm^{-2}·μm^{-1}. The y-axis shows force (raw data) and force per cross-sectional area (in this cell, cross-sectional area was 197 μm^2).

was very difficult to achieve physiological loading largely because of noise in the length signal. Adaptive control, together with zero-delay low-pass filtering, avoided transmission and amplification of noise and successfully circumvented this problem. Furthermore, once the proper command signal could be obtained, the high-intensity illumination for photodiode sensors was not required, allowing the recording of calcium indicator fluorescence for a longer period of time without causing photobleaching.

Study limitations. The major concern with this attachment technique is to avoid damaging the ends of myocytes and to obtain uniform sarcomere spacing (18). Using real-time image analysis, we confirmed that static stretch applied to a resting myocyte could cause uniform stretch of the sarcomere in proportion to cell length. Because of the difficulty in keeping focus on the sarcomere, we could not accurately measure sarcomere length during isometric contractions. However, in the few cases where we could obtain the simultaneous recording of sarcomere length during isometric contraction, internal shortening did take place (Fig. 6*B*). To achieve precise control of sarcomere length, further improvement of the experimental setup may be necessary.

Finally, some myocytes were too irritable to obtain stable recordings, even with streptomycin in the medium as an inhibitor of stretch-activated channels. This might have lead to selection bias of myocytes and disturbed the experiment.

In summary, by adopting digital adaptive control, we studied the mechanics of a rat single cardiac myocyte over a wide range of loading conditions. All of the functional characteristics described were analogous to those established by a number of studies using papillary muscle (4, 6) or trabeculae preparations (7). The present results confirmed the fact that each myocyte forms the functional basis for ventricular function and that single cell mechanics can be a link between subcellular events and ventricular mechanics.

APPENDIX: RELATION BETWEEN LOAD AND LATERAL DISPLACEMENT OF A BEAM

Case A

When lateral force (P) applied to the free end of a cantilever beam [length (*l*)] causes displacement (*y*) (Fig. 8), they are related as

$$y = \frac{\mathrm{P} \cdot l^3}{3 \cdot E \cdot \mathrm{I}} \qquad (A1)$$

or

$$\mathrm{P} = \frac{3 \cdot E \cdot \mathrm{I}}{l^3} \cdot y \qquad (A2)$$

where I is the second moment of inertia of the cross section and *E* is Young's modulus.

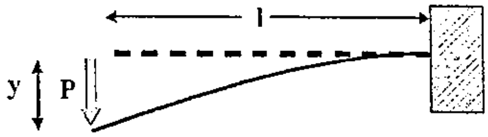

Fig. 8. *Case A*. Lateral force (P) applied to the free end of a cantilever beam [length (*l*)] causes displacement (*y*).

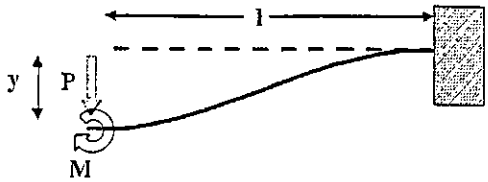

Fig. 9. *Case B*. For the end of fiber to move in parallel manner (without rotation), an appropriate amount of bending moment (M) should also be applied.

For a beam having a circular cross section with diameter *D*

$$\mathrm{P} = \frac{3 \cdot \pi \cdot E \cdot D^4}{64 \cdot l^3} \cdot y \qquad (A3)$$

Case B

For the end of fiber to move in parallel manner (without rotation), an appropriate amount of bending moment (M) should also be applied (Fig. 9). Such a load can be calculated as

$$\mathrm{M} = \frac{\mathrm{P} \cdot l}{2} \qquad (A4)$$

The displacement (*y'*) induced by M is

$$y' = -\frac{\mathrm{M} \cdot l^2}{2 \cdot E \cdot \mathrm{I}} \qquad (A5)$$

Total displacement (y) caused by lateral load P and moment load M is then

$$y = \frac{\mathrm{P} \cdot l^3}{3 \cdot E \cdot \mathrm{I}} - \frac{\mathrm{P} \cdot l^3}{4 \cdot E \cdot \mathrm{I}} = \frac{\mathrm{P} \cdot l^3}{12 \cdot E \cdot \mathrm{I}} \qquad (A6)$$

or

$$\mathrm{P} = \frac{12 \cdot E \cdot \mathrm{I}}{l^3} \cdot y \qquad (A7)$$

Similarly, for a beam having a circular cross section with diameter *D*

$$\mathrm{P} = \frac{12 \cdot \pi \cdot E \cdot D^4}{64 \cdot l^3} \cdot y \qquad (A8)$$

In *case A*, the displacement *y* at *x* from the free end is calculated as

$$y = \frac{\mathrm{P}}{6 \cdot E \cdot \mathrm{I}}(x^3 - 3l^2x + 2l^3) \qquad (A9)$$

or at the distance (*z*) from the fixed end as

$$y = \frac{\mathrm{P}}{6 \cdot E \cdot \mathrm{I}} z^2 \cdot (3l - z) \qquad (A10)$$

In *case B*, the displacement *y* at *x* from the free end is calculated as

$$y = \frac{\mathrm{P}}{12 \cdot E \cdot \mathrm{I}}(l - x)^2 \cdot (l + 2x) \qquad (A11)$$

or at *z* from the fixed end as

$$y = \frac{\mathrm{P}}{12 \cdot E \cdot \mathrm{I}} z^2 \cdot (3l - 2z) \qquad (A12)$$

ACKNOWLEDGMENTS

We thank C. Miyazawa for excellent technical assistance.

GRANTS

This study was supported by grants from the Program for Promotion of Fundamental Studies in Health Sciences of the Organization for Pharmaceutical Safety Research, the Vehicle Racing Commemorative Foundation, the Fugaku Trust for Medical Research, and a Research Grant for Cardiovascular Disease from the Ministry of Health, Labor and Welfare. K. P. Yamada was supported by a Japan Society for the Promotion of Science postdoctoral fellowship for foreign researchers.

REFERENCES

1. **Anversa P and Olivetti G.** Cellular basis of physiological and pathological myocardial growth. In: *Handbook of Physiology. The Cardiovascular System. The Heart.* Bethesda, MD: Am. Physiol. Soc., 2000, sect. 2, vol. I, chapt. 2, p. 75–144.
2. **Bluhm WF, McCulloch AD, and Lew WY.** Active force in rabbit ventricular myocytes. *J Biomech* 28: 1119–1122, 1995.
3. **Brady AJ.** Mechanical properties of isolated cardiac myocytes. *Physiol Rev* 71: 413–428, 1991.
4. **Brady AJ, Tan ST, and Ricchiuti NV.** Contractile force measured in unskinned isolated rat heart fibers. *Nature* 282: 728–729, 1979.
5. **Brooks WW, Bing OH, Blaustein AS, and Allen PD.** Comparison of contractile state and myosin isoenzyme of rat right and left ventricular myocardium. *J Mol Cell Cardiol* 19: 433–440, 1987.
6. **Brutsaert DL and Sonnenblick EH.** Force-velocity-length-time relations of the contractile elements in heart muscle of the cat. *Circ Res* 24: 137–149, 1969.
7. **De Tombe PP and ter Keurs HEDJ.** Force and velocity of sarcomere shortening in trabeculae from rat heart. Effects of temperature. *Circ Res* 66: 1239–1254, 1990.
8. **Del Monte F, Harding SE, Schmidt U, Matsui T, Kang ZB, Dec GW, Gwathmey JK, Rosenzweig A, and Hajjar RJ.** Restoration of contractile function in isolated cardiomyocytes from failing human hearts by gene transfer of SERCA2a. *Circulation* 100: 2308–2311, 1999.
9. **Farmer BB, Mancina M, Williams ES, and Watanabe AM.** Isolation of calcium tolerant myocytes from adult rat hearts: review of the literature and description of a method. *Life Sci* 33: 1–18, 1983.
10. **Fitzsimons DP, Patel JR, and Moss RL.** Role of myosin heavy chain composition in kinetics of force development and relaxation in rat myocardium. *J Physiol* 513: 171–183, 1998.
11. **Garnier D.** Attachment procedures for mechanical manipulation of isolated cardiac myocytes: a challenge. *Cardiovasc Res* 28: 1958–1964, 1994.
12. **Georgakopoulos D and Kass DA.** Minimal force-frequency modulation of inotropy and relaxation of in situ murine heart. *J Physiol* 534: 535–545, 2001.
13. **Guccione JM, LePrell GS, de Tombe PP, and Hunter WC.** Measurement of active myocardial tension under a wide range of physiological loading conditions. *J Biomech* 30: 189–192, 1997.
14. **Janssen PM and de Tombe PP.** Uncontrolled sarcomere shortening increases intracellular Ca^{2+} transient in rat cardiac trabeculae. *Am J Physiol Heart Circ Physiol* 272: H1892–H1897, 1997.
15. **Josephson RA, Spurgeon HA, and Lakatta EG.** The hyperthyroid heart. An analysis of systolic and diastolic properties in single rat ventricular myoyctes. *Circ Res* 66: 773–781, 1990.
16. **Le Guennec JY, Peineau N, Argibay JA, Mongo KG, and Garnier D.** A new method of attachment of isolated mammalian ventricular myocytes for tension recording: length dependence of passive and active tension. *J Mol Cell Cardiol* 22: 1083–1093, 1990.
17. **Michele DE, Albayya FP, and Metzger JM.** Direct, convergent hypersensitivity of calcium-activated force generation produced by hypertrophic cardiomyopathy mutant alpha-tropomyosins in adult cardiac myocytes. *Nat Med* 5: 1413–1417, 1999.
18. **Palmer RE, Brady AJ, and Roos KP.** Mechanical measurement from isolated cardiac myocytes using a pipette attachment system. *Am J Physiol Cell Physiol* 270: C697–C704, 1996.
19. **Peterson JN, Hunter WC, and Berman MR.** Control of segment length or force in isolated papillary muscle: an adaptive approach. *Am J Physiol Heart Circ Physiol* 256: H1726–H1734, 1989.
20. **Regnier M, Lee DM, and Homsher E.** ATP analogs and muscle contraction: mechanics and kinetics of nucleotide tirphosphate binding and hydrolysis. *Biophys J* 74: 3044–3058, 1998.
21. **Stevens C and Hunter PJ.** Sarcomere length change in a 3D mathematical model of the pig ventricle. *Prog Biophys Mol Biol* 82: 229–241, 2003.
22. **Watanabe H, Hisada T, Sugiura S, Okada J, and Fukunari H.** Computer simulation of blood flow, left ventricular wall motion and their interrelationship by fluid-structure interaction finite element method. *JSME Int J* 44: 125–133, 2002.
23. **White E, Boyett MR, and Orchad CH.** The effects of mechanical loading and changes of length on single guinea-pig ventricular myocytes. *J Physiol* 482: 93–107, 1995.
24. **Wu Y, Cazorla O, Labeit D, Labeit S, and Granzier H.** Changes in titin and collagen underlie diastolic stiffness diversity of cardiac muscle. *J Mol Cell Cardiol* 32: 2151–2162, 2000.
25. **Yasuda S, Sugiura S, Yamashita H, Nishimura S, Saeki Y, Momomura S, Katoh K, Nagai R, and Sugi H.** Unloaded shortening increases the peak of Ca^{2+} transients but accelerates their decay in rat single cardiac myocytes. *Am J Physiol Heart Circ Physiol* 285: H470–H475, 2003.
26. **Yasuda SI, Sugiura S, Kobayakawa N, Fujita H, Yamashita H, Katoh K, Saeki Y, Kaneko H, Suda Y, Nagai R, and Sugi H.** A novel method to study contraction characteristics of a single cardiac myocyte using carbon fibers. *Am J Physiol Heart Circ Physiol* 281: H1442–H1446, 2001.
27. **Yoneda M.** Force exerted by a single cilium of *Mytilus edulus*. *J Exp Biol* 37: 461–468, 1960.

Am J Physiol Regul Integr Comp Physiol 286: R844–R850, 2004.
First published December 30, 2003; 10.1152/ajpregu.00497.2003.

Bed rest attenuates sympathetic and pressor responses to isometric exercise in antigravity leg muscles in humans

Atsunori Kamiya,[1,2] Daisaku Michikami,[1,2] Tomoki Shiozawa,[3] Satoshi Iwase,[2] Junichiro Hayano,[4] Toru Kawada,[1] Kenji Sunagawa,[1] and Tadaaki Mano[2]
[1]*Department of Cardiovascular Dynamics, National Cardiovascular Center Research Institute, Osaka 565–8565;* [2]*Department of Autonomic Neuroscience, Research Institute of Environmental Medicine, Nagoya University, Nagoya 464–8601;*
[3]*Department of Hygiene and Space Medicine, Nihon University School of Medicine, Tokyo 173–8610; and*
[4]*Core Laboratory, Nagoya City University Graduate School of Medical Sciences, Nagoya 467–8601, Japan*

Submitted 29 August 2003; accepted in final form 24 December 2003

Kamiya, Atsunori, Daisaku Michikami, Tomoki Shiozawa, Satoshi Iwase, Junichiro Hayano, Toru Kawada, Kenji Sunagawa, and Tadaaki Mano. Bed rest attenuates sympathetic and pressor responses to isometric exercise in antigravity leg muscles in humans. *Am J Physiol Regul Integr Comp Physiol* 286: R844–R850, 2004. First published December 30, 2003; 10.1152/ajpregu.00497.2003.—Although spaceflight and bed rest are known to cause muscular atrophy in the antigravity muscles of the legs, the changes in sympathetic and cardiovascular responses to exercises using the atrophied muscles remain unknown. We hypothesized that bed rest would augment sympathetic responses to isometric exercise using antigravity leg muscles in humans. Ten healthy male volunteers were subjected to 14-day 6° head-down bed rest. Before and after bed rest, they performed isometric exercises using leg (plantar flexion) and forearm (handgrip) muscles, followed by 2-min postexercise muscle ischemia (PEMI) that continues to stimulate the muscle metaboreflex. These exercises were sustained to fatigue. We measured muscle sympathetic nerve activity (MSNA) in the contralateral resting leg by microneurography. In both pre- and post-bed-rest exercise tests, exercise intensities were set at 30 and 70% of the maximum voluntary force measured before bed rest. Bed rest attenuated the increase in MSNA in response to fatiguing plantar flexion by ~70% at both exercise intensities (both $P < 0.05$ vs. before bed rest) and reduced the maximal voluntary force of plantar flexion by 15%. In contrast, bed rest did not alter the increase in MSNA response to fatiguing handgrip and had no effects on the maximal voluntary force of handgrip. Although PEMI sustained MSNA activation before bed rest in all trials, bed rest entirely eliminated the PEMI-induced increase in MSNA in leg exercises but partially attenuated it in forearm exercises. These results do not support our hypothesis but indicate that bed rest causes a reduction in isometric exercise-induced sympathetic activation in (probably atrophied) antigravity leg muscles.

autonomic nervous system; deconditioning; inactivity; muscle atrophy; microneurography; sympathetic nerve activity

EXPOSURES TO SPACEFLIGHT (11, 25) and its simulation model, 6° head-down bed rest (6, 8, 9), are known to cause cardiovascular deconditioning in humans. Although the primary symptom of the deconditioning is orthostatic intolerance on return to Earth (2, 6, 25), deconditioning may also include a reduction in sympathetic and cardiovascular responses to isometric exercise (15, 21). For example, bed rest attenuates the increase in arterial pressure and heart rate in response to static handgrip exercise (15, 21). While some studies suggest that these responses are reduced after spaceflight (179–389 days) (21), a more recent study on the effects of spaceflight (16 days) failed to confirm this observation (7). However, most of these studies investigated exercises using forearm muscles that were not affected by spaceflight and bed rest.

Contrary to the situation of forearm muscles, exposure to spaceflight and bed rest causes muscular atrophy in the antigravity muscles of the legs (3, 5, 17). This is associated with various changes in muscular tissues, including decreases in myofiber size (3, 5, 17), capillary volume (3, 4), mitochondrial volume density (4), and muscle oxidative capacity (3–5). Although astronauts in space and hospitalized patients confined to bed must use their atrophied antigravity leg muscles on return to daily life, particularly in standing and walking, little is known regarding changes in the sympathetic and cardiovascular responses to exercise using these atrophied leg muscles after spaceflight and bed rest. These changes may relate to the integrative physiological effects of microgravity on human cardiovascular and musculoskeletal systems.

In our earlier study (8), we found that 14-day bed rest did not change muscle sympathetic nerve activity (MSNA) during isometric forearm exercise (handgrip) but mildly reduced MSNA during postexercise muscle ischemia (PEMI) that continues to stimulate the muscle metaboreflex (16, 20). Because the muscle metaboreflex activation is due to muscle metabolic responses (16, 20), it is likely that the reflex is more activated in antigravity atrophied leg muscles that would elicit a greater disturbance in metabolic responses to exercises (3, 5). Accordingly, we hypothesized that bed rest would augment sympathetic responses to isometric exercise using antigravity leg muscles in humans. We subjected 10 healthy male volunteers to a 14-day period of bed rest. Bed rest is known to induce an ~10% reduction in maximal voluntary contraction (MVC) of antigravity leg muscles but does not affect forearm muscles (3). We performed isometric fatiguing exercises with leg (plantar flexion) and forearm (handgrip) muscles, followed by 2 min of PEMI, with measuring MSNA in the contralateral resting leg by the microneurographic technique.

MATERIALS AND METHODS

Subjects

Ten healthy male volunteers with a mean age (±SE) of 22 ± 1 yr, mean height (±SE) of 168 ± 2 cm, and mean weight (±SE) of 64 ±

Address for reprint requests and other correspondence: A. Kamiya, Dept. of Cardiovascular Dynamics, National Cardiovascular Center Research Institute, 5-7-1 Fujishirodai, Suita, Osaka 565-8565, Japan (E-mail: kamiya@ri.ncvc.go.jp).

3 kg participated in this study. We evaluated all subjects as healthy by completing a detailed medical history and by conducting a physical examination, resting electrocardiogram, blood chemistry analyses, and psychological testing. None of the subjects smoked or had experience of recreational drugs. All subjects were righthanded. All subjects gave informed consent to participate in this study, which was approved by the Ethical Committee of the National Space Development Agency of Japan and the Committee of Human Research, Research Institute of Environmental Medicine, Nagoya University.

Bed-Rest Protocols

The volunteers were subjected to 14 days of 6° head-down bed rest. The experimental bed-rest room was air-conditioned at a temperature of 25–26°C and relative humidity of 30–40%. Physical exercise and drinking of caffeinated and alcoholic beverages were prohibited throughout the bed-rest period. During bed rest, staff nurses continuously monitored subjects to ensure that they remained in the 6° head-down position and performed no physical exercise. Dietary intake was restricted to between 2,000 and 2,100 kcal/day (55% carbohydrate, 25% fat, 20% protein), including ~3,000 mg/day of sodium. Fluid intake from daily drinks was ad libitum, and the average was 1.261 ± 83 ml/day. The light-dark cycle was 16 h of light and 8 h of darkness with lights on at 0700.

Experimental Protocol of Forearm and Leg Isometric Exercise Tests

Tests before bed rest. Two to three weeks before bed rest, we conducted pre-bed-rest forearm and leg exercise tests. We instructed the subjects to refrain from eating for 3 h before the experiments. Each subject was positioned horizontally supine on a bed equipped with a plate containing a strain-gauge transducer (LP-200KB, WGA-710A-4, Kyowa Electronic Instruments, Tokyo, Japan) for the measurement of contraction force generated in the right leg. We fixed the ankle and the metatarsal head of the right foot to this plate using nonelastic strips, setting the ankle at an angle of 90°. The elbow of the right arm was almost fully extended. We placed a handgrip dynamometer (Digital Grip Dynamometer, Takei Kiki Kogyo, Japan) on the right hand for each subject to grip. Each subject performed brief (<5 s) muscle contraction exercises four times: two handgrips and two plantar flexions, with all his strength. Each contraction was done separately, with intervals of at least 10 min between contractions. The average values of the two handgrips and plantar flexions were used as the MVC forces for the forearm and leg exercises, respectively.

After these exercises, each subject remained supine and rested for >30 min. At least 20 min after a satisfactory recording site for microneurography (the tibial nerve at the left popliteal fossa) was found, we obtained preexercise baseline measurements of the variables over a period of 5 min. The subjects then performed isometric exercises of right handgrip (forearm exercise test) and right plantar flexion (leg exercise test) separately, sustaining the contraction to the point of fatigue. In both forearm and leg exercises, we set two levels of contraction intensity: 30 and 70% of the MVC forces. Forearm and leg exercise tests were performed alternately at intervals of at least 20 min. In forearm or leg exercise, 30 and 70% MVC exercises were done in random order. We used an oscilloscope to display to the exercising subject the target force and the achieved output from a handgrip dynamometer or foot plate transducer. When the achieved output declined to <85% of the target force for >2 s, we inflated the arterial pressure cuff around the right upper arm (for forearm exercise) or the right thigh (for leg exercise) to a suprasystolic arterial pressure of 230 mmHg with a lag of 3 s and terminated the exercise after 3 s. This produced PEMI and was sustained for 2 min. The PEMI was intended to trap muscle metabolites and thereby continue stimulating the muscle metaboreflex to maintain the MSNA (16, 20). During all exercise tests, we regulated the subject's breathing using a metronome (Digital Metronome MA-20, Korg, Tokyo). We required the subjects to breathe 15 times/min with expiration and inspiration phases of 2 s each. We also required them to avoid breathing deeply or to perform Valsalva maneuvers. In addition, we directed them to avoid contracting other limbs. We measured the variables continuously during the preexercise control period, exercise, PEMI, and recovery.

Tests after bed rest. Immediately after the bed-rest period, we conducted post-bed-rest forearm and leg exercise tests. Subjects were positioned horizontally supine on the bed. We determined MVC forces of handgrip and plantar flexion in the same manner as before bed rest. We also performed forearm and leg exercise tests in an identical manner to those before bed rest. All exercise tests after bed rest were conducted at the same intensities as before bed rest (30 and 70% of the MVC force obtained before, and not after, bed rest). As a result, in the leg exercise tests, the exercise intensity was similar in absolute terms but higher in relative terms after bed rest than before bed rest, because bed rest decreased the MVC force of plantar flexion. In contrast, in the forearm exercise tests, the exercise intensity was similar in both relative and absolute terms before and after bed rest, because bed rest did not change the MVC force of handgrip.

Measurements. MSNA was measured from the tibial nerve of the left resting leg as reported previously (12, 24). Briefly, a tungsten microelectrode (model 26–05–1, Haer, Bowdoinham, ME) was inserted percutaneously into the muscle nerve fascicles of the tibial nerve at the left popliteal fossa without anesthesia. Nerve signals were fed into a preamplifier (Kohno Instruments, Nagoya, Japan) with two active band-pass filters set between 500 and 5,000 Hz and were subsequently monitored with a loudspeaker. MSNA was identified according to the following discharge characteristics: *1*) arterial pulse synchronous spontaneous efferent discharges, *2*) afferent activity induced by tapping of calf muscles but not in response to gentle skin touch, and *3*) enhancement during phase II of the Valsalva maneuver. We stored the MSNA signals on a DAT recorder (PC216Ax, Sony Magnescale) at a sampling rate of 12,000 Hz, together with other cardiovascular variables.

We measured arterial pressure continuously with a pneumatic finger cuff on the left arm with periodical calibrating (Portapres, TNO Institute of Applied Physics Biomedical Instrumentation) (26). The mean arterial pressure was calculated as the diastolic arterial pressure plus one-third of the pulse pressure. In a preliminary experiment without bed rest, we compared the Portapres finger pressure with simultaneously measured right brachial arterial pressure (BP203MII, Nippon Colin) every minute during leg exercises (plantar flexion at 30 and 70% of MVC, $n = 6$). In the experiment, every 1-min mean finger pressure was identical to every corresponding 1-min mean brachial pressure ($r = 0.97$, $P < 0.05$), verifying that the Portapres finger pressure accurately reflects arterial pressure.

A 20-gauge intravenous catheter was inserted into the antecubital vein in the left forearm. Venous blood samples were obtained for determination of plasma lactate concentration before baseline, at rest, and during the 3rd min of the recovery period for each trial.

Data analysis. The full-wave rectified MSNA signal was fed through a resistance-capacitance low-pass filter at a time constant of 0.1 s to obtain the mean voltage neurogram. This was then resampled at 1,000 Hz together with other cardiovascular variables. MSNA bursts were identified and their areas calculated using a computer program custom built by our laboratory. MSNA was expressed as both the rate of integrated activity per minute (burst rate) and the total activity, by integrating individual burst area per minute (total MSNA). Because the burst area and hence the total MSNA were dependent on electrode position, they were expressed as an arbitrary unit (AU) that was normalized by the individual control value before exercise (an average total MSNA per minute during 5 min of preexercise rest was given an arbitrary value of 100). The burst area of each burst during experimental procedures was normalized to this value.

Heart rate was determined from the electrocardiogram. Values of MSNA (burst rate and total activity), mean arterial pressure, heart rate, and respiratory rate were averaged for each 5 min of preexercise baseline. Values were also averaged for the appropriate periods in each exercise test in accordance with the duration sustained to fatigue. For the variables during exercise, the values were averaged every minute for 70% MVC leg exercise (in Fig. 2, Ex 1 and Ex 2 indicate mean values for 0–60 s and 61–120 s, respectively, of exercise) and 30% MVC forearm exercise. The values during exercise were also averaged every 5 min for 30% MVC leg exercise, and every 30 s for 70% MVC forearm exercise (in Fig. 3, Ex 1 and Ex 2 indicate mean values for 0–30 s and 31–60 s, respectively, of exercise). Value at the point of fatigue was the average for the last 20 s of exercise. The average values for the last 60 s of PEMI and recovery were also calculated.

Statistical Analysis

Data are expressed as means ± SE. Repeated-measures ANOVA was used to compare variables for condition (before and after bed rest) and time [baseline, *exercise 1* (first half), *exercise 2* (second half), fatigue, PEMI, and recovery]. When the main effect or interaction term was found to be significant, post hoc comparisons were made using the Scheffé's *F*-procedure. A Wilcoxon signed-rank test was used to compare variables (MVC forces of handgrip and plantar flexion and greatest circumferences of the forearm and the calf) before and after bed rest. We considered $P < 0.05$ to be statistically significant.

RESULTS

Bed rest did not change the strength of MVC force of handgrip (411.7 ± 27.1 N before bed rest and 408.3 ± 29.4 N after) but reduced that of plantar flexion from 861.7 ± 43.0 to 755.2 ± 42.8 N ($P < 0.05$). Bed rest did not change the maximal circumference length of the forearm (26.1 ± 0.8 cm before and 25.9 ± 0.8 cm after) but reduced that of the calf from 36.2 ± 0.8 to 34.1 ± 0.7 cm ($P < 0.05$). Bed rest did not change baseline MSNA burst rate, heart rate, or mean arterial pressure (see Figs. 2 and 3).

Leg exercise test (plantar flexion). At 70% MVC, the duration of leg exercise sustained to the point of fatigue was 151 ± 9 s before bed rest and 147 ± 8 s after bed rest. Figure 1 illustrates a representative microneurographic recording of MSNA in a typical subject performing 70% MVC leg exercise. Although leg exercise and the subsequent PEMI strongly increased MSNA before bed rest, these increases were attenuated markedly after bed rest. The average data of all subjects showed that although leg exercise increased MSNA both before and after bed rest, the increase was markedly reduced after bed rest ($P < 0.05$ vs. before bed rest, Fig. 2). Before bed rest, PEMI decreased MSNA ($P < 0.05$ vs. end of the exercise) but maintained it at an elevated level relative to the preexercise baseline. After bed rest, however, PEMI failed to maintain the MSNA, resulting in a return to the baseline level (Fig. 2). These results indicated that bed rest abolished the PEMI-induced increases in MSNA after leg exercise.

In 70% MVC leg exercise, the effects of bed rest on mean arterial pressure during leg exercise and PEMI were consistent with those for MSNA (Fig. 2). Although leg exercise increased mean arterial pressure both before and after bed rest, the increase was smaller after bed rest ($P < 0.05$ vs. before bed rest, Fig. 2). PEMI decreased mean arterial pressure ($P < 0.05$ vs. end of the exercise) but maintained it above the baseline level ($P < 0.05$ vs. baseline) before bed rest, whereas the pressure returned to base-

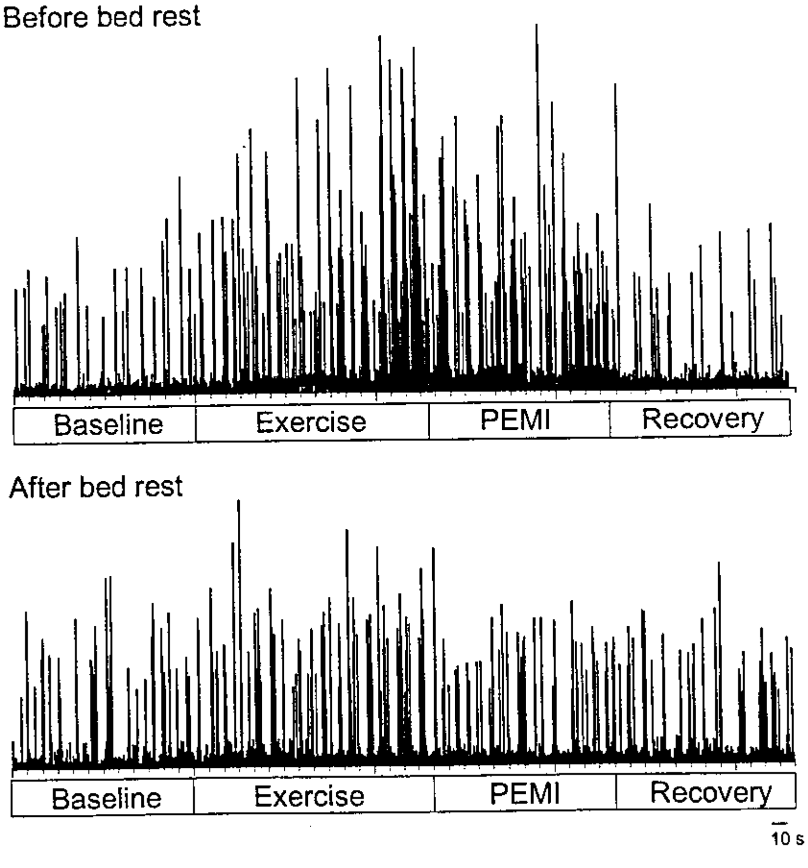

Fig. 1. Representative microneurographic recording of muscle sympathetic nerve activity (MSNA) from a typical subject during leg exercise (plantar flexion) test at 70% maximal voluntary contraction (MVC) force sustained to the point of fatigue performed before and after bed rest. Baseline, before contraction (time: 2 min, before and after bed rest); exercise, plantar flexion at 70% MVC sustained to fatigue (time: 155 s before bed rest, and 160 s after bed rest); postexercise muscle ischemia (PEMI; time: 2 min, before and after bed rest); recovery (time: 2 min, before and after bed rest). Exercise induced increases in MSNA during exercise and PEMI before bed rest, but these increases were attenuated after bed rest.

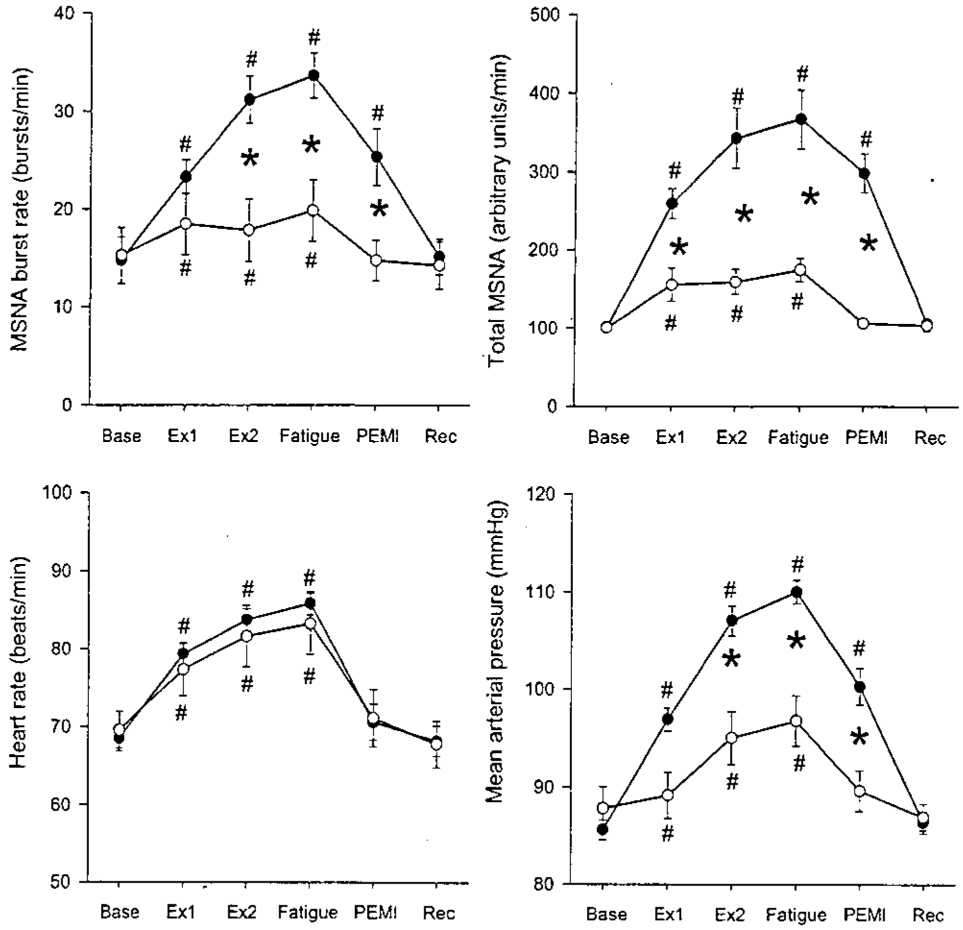

Fig. 2. Changes in MSNA burst rate (*top left*), total MSNA (*top right*), heart rate (*bottom left*), and mean arterial pressure (*bottom right*) during leg exercise (plantar flexion) at 70% MVC force sustained to the point of fatigue. Base, baseline before exercise; Ex1, 1st min (0–60 s) of exercise; Ex2; 2nd min (61–120 s) of exercise; Fatigue, point of fatigue (last 20 s of exercise); PEMI, 2nd min (61–120 s) of PEMI; Rec, 2nd min (61–120 s) of recovery. ● and ○, Values before and after bed rest, respectively. Values are means ± SE. $*P < 0.05$ comparing before and after bed rest. $\#P < 0.05$ vs. preexercise baseline values.

line after bed rest (Fig. 2). Bed rest did not significantly affect heart rate during leg exercise (Fig. 2). Both before and after bed rest, respiratory rate was almost constant at 15 cycles/min throughout rest, leg exercise, PEMI, and recovery. Leg exercise at 70% MVC increased plasma lactate concentration similarly before and after bed rest (from 1.0 ± 0.1 to 2.7 ± 0.1 mmol/ml before bed rest and 0.9 ± 0.1 to 2.8 ± 0.1 mmol/ml after bed rest).

The effects of bed rest on MSNA, mean arterial pressure, and heart rate in 30% MVC leg exercise were similar to those observed in 70% MVC leg exercise. The duration of exercise sustained to the point of fatigue was similar before (684 ± 18 s) and after (673 ± 18 s) bed rest. Bed rest attenuated MSNA during the first 10 min of exercise and at fatigue both in burst rate (from 34 ± 2 to 21 ± 2 bursts/min, $P < 0.05$) and total activity [from 363 ± 321 to 166 ± 17 AU, $P < 0.05$]. Although PEMI maintained the elevated MSNA burst rate (14 ± 3 bursts/min) and total activity (227 ± 29 AU) above baseline before bed rest, the PEMI-induced elevation of MSNA disappeared after bed rest. Similarly, PEMI-induced increases in mean arterial pressure seen before bed rest (24 ± 2 mmHg) were abolished after bed rest. Bed rest did not affect responses of heart rate and respiratory rate. Leg exercise at 30% MVC increased plasma lactate concentration similarly before and after bed rest (from 0.9 ± 0.1 and 2.9 ± 0.1 mmol/ml before bed rest and 0.8 ± 0.1 to 2.9 ± 0.1 mmol/ml after bed rest).

Forearm exercise test (handgrip). The duration of exercise sustained to fatigue was similar before and after bed rest in forearm exercise at 70% (77 ± 9 and 75 ± 7 s, before and after bed rest, respectively) and 30% MVC (153 ± 11 and 147 ± 9 s). In contrast to leg exercises, forearm exercise increased MSNA and mean arterial pressure similarly before and after bed rest both at 30 and 70% MVC (Fig. 3). PEMI maintained MSNA at elevated levels above baseline before and after bed rest ($P < 0.05$ vs. baseline); however, the increases during PEMI were reduced after bed rest at 30% MVC (from 241 ± 32 to 150 ± 29 AU) and 70% MVC (Fig. 3) ($P < 0.05$ at both intensities). PEMI-induced increase in mean arterial pressure was also lower after bed rest in forearm exercise at 30% (from 22 ± 3 to 10 ± 3 mmHg) and 70% MVC (Fig. 3) ($P < 0.05$ at both intensities). Bed rest did not affect heart rate during forearm exercise (Fig. 3). Both before and after bed rest, respiratory rate was almost constant at 15 cycles/min throughout rest, forearm exercise, PEMI, and recovery. Forearm exercises increased plasma lactate concentration similarly before and after bed rest, at both 30% (from 0.9 ± 0.1 to 3.1 ± 0.1 mmol/ml before bed rest; from 0.8 ± 0.1 to 3.2 ± 0.1 mmol/ml after bed rest) and 70% MVC (from 1.0 ± 0.1 to 2.8 ± 0.1 mmol/ml before bed rest; from 0.9 ± 0.1 to 2.9 ± 0.1 mmol/ml after bed rest).

DISCUSSION

Reduced MSNA and Pressor Responses to Antigravity Leg Exercise After Bed Rest

Although spaceflight and bed rest are known to cause muscular atrophy in antigravity muscles in legs, changes in sympathetic and cardiovascular responses to exercise using the

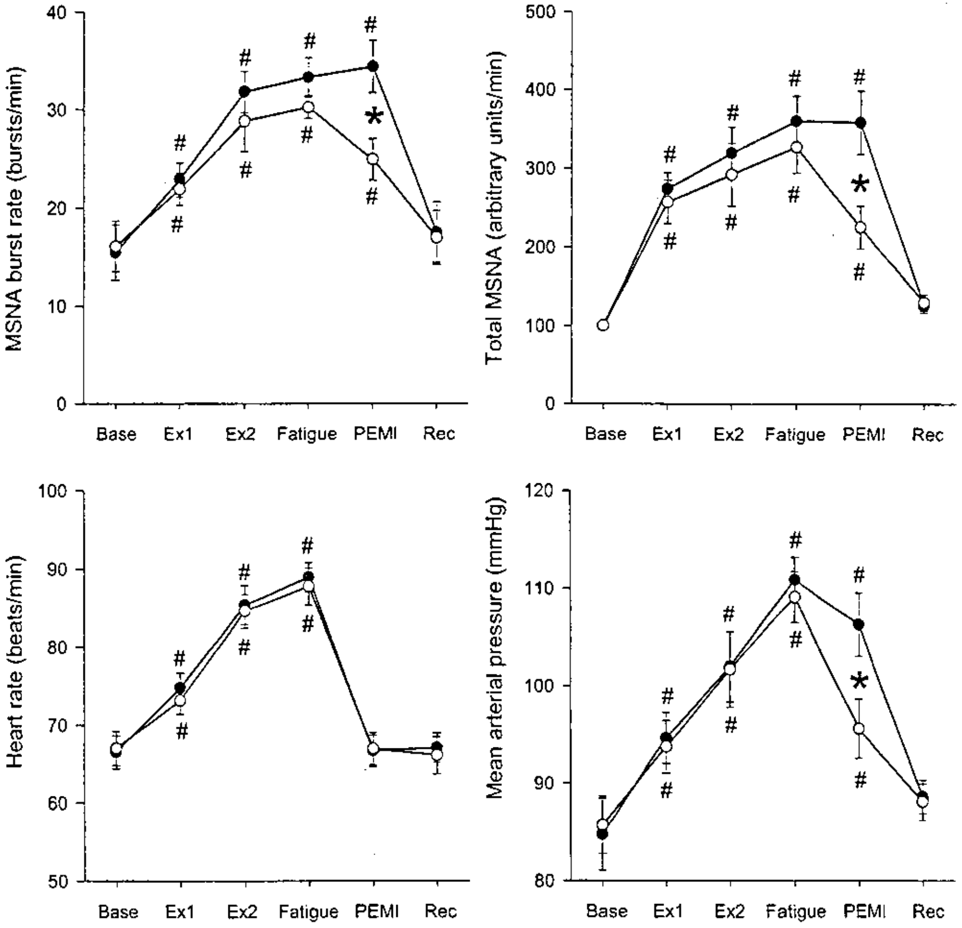

Fig. 3. Changes in MSNA burst rate (*top left*), total MSNA (*top right*), heart rate (*bottom left*), and mean arterial pressure (*bottom right*) during forearm exercise (handgrip) at 70% of MVC force sustained to the point of fatigue. Base, baseline before exercise; Ex1, 1st half (0–30 s) of exercise; Ex2, 2nd half (31–60 s) of exercise; Fatigue, point of fatigue (last 20 s of exercise); PEMI, 2nd min (61–120 s) of PEMI; Rec, 2nd min (61–120 s) of recovery. ● and ○, Values before and after bed rest, respectively. Values are means ± SE. $*P < 0.05$ comparing before and after bed rest. $\#P < 0.05$ vs. preexercise baseline values.

atrophied muscles remain unknown. Given a possible greater disturbance in metabolic response to exercise in atrophied muscles, we hypothesized that bed rest would augment sympathetic responses to isometric exercise using antigravity leg muscles in humans. The new finding of the present study is that 14-day bed rest attenuated MSNA and pressor responses to fatiguing isometric plantar flexion by ~70% and reduced the MVC force of plantar flexion by 15%. In contrast, bed rest did not alter MSNA and pressor responses to fatiguing isometric handgrip and had no effect on the MVC force of handgrip, which are consistent with previous studies (7, 8). These results do not support our hypothesis. They indicate that bed rest causes a reduction in isometric exercise-induced sympathetic activation in (probably atrophied) antigravity leg muscles.

The most likely mechanism responsible for the attenuated MSNA responses to isometric exercise in antigravity leg muscles after bed rest is the absence or strong reduction of activation of the muscle metaboreflex. The muscle metaboreflex is known to play a primary role in MSNA response to exercise (14, 16, 20). We assessed the reflex during PEMI because this method traps muscle metabolites in muscles that have undergone exercise and continues to stimulate the muscle metaboreflex but not other reflexes (such as the muscle mechanoreflex, central command) (14, 16, 20). Our present pre-bed-rest data confirmed the importance of the reflex because MSNA remained elevated from the preexercise level during PEMI. However, of special note is the fact that the sustained increase in MSNA by PEMI disappeared after bed rest (Fig. 2). This result indicates that bed rest almost abolishes the activation of the muscle metaboreflex in antigravity leg muscles.

Our data showed that heart rate responses to leg exercises did not change after bed rest despite the attenuated increases in MSNA. It was possible that cardiac vagal responses to exercise might be augmented after bed rest, compensating for the reduced cardiac sympathetic neural responses and resulting in normal heart rate responses.

We do not consider the attenuated MSNA and pressor responses to exercises observed in this study as simple accommodations to the tests. In preliminary experiments, we repeated exercise tests with identical protocols to the present study (n = 6; 30 and 70% MVC handgrip, 30 and 70% MVC plantar flexion) with an interval of 2 wk of non-bed-rest period. We confirmed the reproducibility of sympathetic and cardiovascular responses because these responses were almost identical between the first and second trials with a correlation coefficient of ~0.9.

Comparison of forearm and antigravity leg exercises. Bed rest exerts different effects on forearm and antigravity leg muscles in MSNA and pressor responses to fatiguing isometric exercise. First, activation of the muscle metaboreflex was only mildly reduced in forearm muscles, in contrast to entire disappearance in antigravity leg muscles. MSNA and pressor responses during PEMI were ~50% lower after bed rest in handgrip exercises both at 30 and 70% of MVC, consistent with our earlier studies using 30% MVC handgrip (8). Although the reduction of the muscle metaboreflex in handgrip was not observed in the NeuroLab (STS-90) space shuttle mission study (7), this could be explained by the methodological difference of spaceflight vs. bed rest.

Second, total responses of MSNA and arterial pressure to fatiguing isometric handgrip in forearm muscles were preserved after bed rest, in contrast to the greatly attenuated responses in antigravity leg muscles. Our finding of forearm exercises was consistent with the results of earlier studies of bed rest (8, 23) and also a recent study from NeuroLab (STS-90) space shuttle mission (7). However, our finding of forearm exercises disagreed with earlier studies by Spaak et al. (21) and Pagani et al. (15) that showed the reduced heart rate and arterial pressure responses to handgrip at 25–30% MVC. The discrepancy may be explained by the difference in the exercise mode: handgrip sustained to fatigue in our study vs. handgrip for fixed durations in their studies (2 and 5 min). An important point is that sympathetic activation during static handgrip directly relates to the development of fatigue (18, 19) and peaks at fatigue (19). Therefore, their methodology of fixed exercise duration may limit and complicate the interpretation of data. Because, generally, muscle strength (MVC) does not equate to endurance, it may not predict well the activation of muscle metaboreflex during exercise. Another factor is the duration of spaceflight or bed rest. Compared with the present study (14 days), longer term bed rest [42 days (15) and 120 days (21) days] and spaceflight (179–389 days) (21) were conducted in their studies. Long- and short-term exposures to microgravity could have different effects on sympathetic and cardiovascular responses to exercise.

Mechanisms for Reduced Activations of the Muscle Metaboreflex After Bed Rest

Again, our results of MSNA and pressor responses during PEMI showed that bed rest abolished the activation of muscle metaboreflex in antigravity leg muscles and mildly attenuated the activation in forearm muscles. However, it is difficult to determine which mechanism in the reflex circuit is responsible for the difference in muscle metaboreflex activation. We propose several possibilities. The first possibility is altered central modulation related to immobilization during bed rest. Bed rest did not change maximal handgrip force and thus is unlikely to have deconditioned forearm muscles. However, the activation of muscle metaboreflex was smaller after bed rest even in the forearm muscles. Accordingly, factors other than muscles, particularly changes in central processing in relation to immobilization, could be responsible in part for the reduced activation of the muscle metaboreflex. This postulation might explain why a recent space shuttle mission study reported by NeuroLab (STS-90) failed to observe reduced MSNA during PEMI (7) because astronauts are highly active in the space shuttle whereas the subjects in our bed-rest study were clearly immobilized. In addition, this explanation could relate to the interesting earlier finding that muscle metaboreceptor responses are attenuated in heart failure patients (22) who are likely to be immobilized or restricted in daily life activities compared with healthy persons.

The second possibility is changes in muscle afferent sensitivity in atrophied leg muscles after bed rest. Given the total disappearance of muscle metaboreflex activation in antigravity leg muscles compared with partial reduction in forearm muscles, factors specific to antigravity muscles could contribute to the reduced activation in muscle metaboreflex. Muscular atrophy (deconditioning) is an obvious possibility. Changes in muscle afferent sensitivity in atrophied muscles rather than alterations in metabolic factors could be responsible for the reduced activation of muscle metaboreflex, because accumulation of exercise-induced metabolites might be increased rather than decreased in atrophied muscles. Indeed, our data showed that bed rest did not reduce plasma lactate concentrations in leg exercises. Accordingly, we speculate that the sensitivity and/or number of metabosensitive receptors on afferent fibers (group III and IV) (20) is reduced in antigravity atrophied leg muscles after bed rest. In addition to decreases in myofiber size (3, 5, 17) and capillary volume (3, 4) in muscular tissues, muscular atrophy is accompanied by reduced muscle spindle afferent sensitivity in soleus muscle after hindlimb suspension in rats (rodent model of microgravity) (1). Unfortunately, little is known regarding changes in metabosensitive muscle afferent fibers in atrophied muscles. Further studies are required to investigate this possibility.

Hypoperfusion to contracting muscles may not account for the reduced activation of muscle metaboreflex in forearm and leg muscles after bed rest. In a previous study, 14-day bed rest reduced resting blood flow to upper and lower limbs (10) and thus could reduce perfusion to exercising limb muscles. However, this would not be responsible for our findings because hypoperfusion induced by arm elevation increased, instead of decreased, MSNA activation during PEMI after isometric handgrip (13).

Clinical Implications

In severe clinical conditions including pelvis and femur bone fracture, spinal cord injury, and severe cardiac failure, hospitalized patients are confined to bed for several weeks. Because the bed rest often decreases muscular performance particularly in antigravity leg muscles, exercise has been conducted in hospitals to improve muscular performance as post-bed-rest rehabilitation. However, little attention has been given to the accompanying sympathetic and pressor responses to the exercises in deconditioned or atrophied muscles, even though greater sympathetic excitation is a substrate for cardiovascular events, including ventricular arrhythmia and stroke. Our finding suggests that post-bed-rest rehabilitation has a minor risk of enhanced sympathetic excitation because MSNA responses to exercise in antigravity leg muscles are reduced, rather than increased, after bed rest.

Limitations

Fourteen-day bed rest is known to cause muscular atrophy in antigravity leg muscles (3, 5, 17). Our 14-day bed rest reduced the MVC force of plantar flexion by 15% and the maximal circumference length of the calf by 2.1 cm. Accordingly, we presume that the antigravity calf muscles might be atrophied by bed rest. However, we lack direct evidence of muscular atrophy. We found no earlier fatigue (3, 5) or greater metabolic response to the leg isometric exercise. Leg circumference changes could be affected by fluid shifts (6), whereas muscle strength changes could be influenced by neuromotor change. Further histochemical and morphological investigations on muscular atrophy are required in studies assessing cardiovascular deconditioning after microgravity.

In conclusion, 14-day bed rest attenuated MSNA and pressor responses during the fatiguing exercise and PEMI periods strongly when the isometric contractions were performed by the legs (plantar flexion) but mildly and only during the PEMI periods when performed by the forearm (handgrip). The bed rest reduced the MVC force of plantar flexion but not that of handgrip. These results indicate that bed rest causes a reduction in isometric exercise-induced sympathetic activation in (probably atrophied) antigravity leg muscles.

GRANTS

This study was conducted as a part of "Ground Research Announcement for Space Utilization" promoted by the Japan Space Forum. The study was supported by Grant-in-Aid for Scientific Research (grant no. 13770032) from the Ministry of Education, Science, Sport, and Culture of Japan.

REFERENCES

1. **Anderson J, Almeida-Silveira MI, and Perot C.** Reflex and muscular adaptations in rat soleus muscle after hindlimb suspension. *J Exp Biol* 202: 2701–2707, 1999.
2. **Buckey JC, Lane LD, Levine BD, Watenpaugh DE, Wright SJ, Moore WE, Gaffney FA, and Blomqvist CG.** Orthostatic intolerance after spaceflight. *J Appl Physiol* 81: 7–18, 1996.
3. **Edgerton VR and Roy RR.** Neuromuscular adaptations to actual and simulated spaceflight. In: *Handbook of Physiology. Environmental Physiology. The Gravitational Environment.* Bethesda, MD: Am. Physiol. Soc., 1996, sect. 4, vol. I, chapt. 32, p. 721–756.
4. **Ferretti G, Antonutto G, Denis C, Hoppeler H, Minetti AE, Narici MV, and Desplanches D.** The interplay of central and peripheral factors in limiting maximal O_2 consumption in man after prolonged bed rest. *J Physiol* 501: 677–686, 1997.
5. **Fitts RH, Riley DR, and Widrick JJ.** Physiology of a microgravity environment invited review: microgravity and skeletal muscle. *J Appl Physiol* 89: 823–839, 2000.
6. **Fortney SM, Schneider VS, and Greenleaf JE.** The physiology of bed rest. In: *Handbook of Physiology. Environmental Physiology.* Bethesda, MD: Am. Physiol. Soc., 1996, sect. 4, vol. II, chapt. 39, p. 889–939.
7. **Fu Q, Levine BD, Pawelczyk JA, Ertl AC, Diedrich A, Cox JF, Zuckerman JH, Ray CA, Smith ML, Iwase S, Saito M, Sugiyama Y, Mano T, Zhang R, Iwasaki K, Lane LD, Buckey JC Jr, Cooke WH, Robertson RM, Baisch FJ, Blomqvist CG, Eckberg DL, Robertson D, and Biaggioni I.** Cardiovascular and sympathetic neural responses to handgrip and cold pressor stimuli in humans before, during and after spaceflight. *J Physiol* 544: 653–664, 2002.
8. **Kamiya A, Iwase S, Michikamia D, Fu Q, and Mano T.** Muscle sympathetic nerve activity during handgrip and post-handgrip muscle ischemia after exposure to simulated microgravity in humans. *Neurosci Lett* 280: 49–52, 2000.
9. **Kamiya A, Michikami D, Fu Q, Iwase S, Hayano J, Kawada T, Mano T, and Sunagawa K.** Pathophysiology of orthostatic hypotension after bed rest: paradoxical sympathetic withdrawal. *Am J Physiol Heart Circ Physiol* 285: H1158–H1167, 2003.
10. **Kamiya A, Michikami D, Iwase S, Hayano J, Kawada T, Sugimachi M, and Sunagawa K.** α-Adrenergic vascular responsiveness to sympathetic nerve activity is intact after head-down bed rest in humans. *Am J Physiol Regul Integr Comp Physiol* 286: R151–R157, 2004.
11. **Levine BD, Pawelczyk JA, Ertl AC, Cox JF, Zuckerman JH, Diedrich A, Biaggioni I, Ray CA, Smith ML, Iwase S, Saito M, Sugiyama Y, Mano T, Zhang R, Iwasaki K, Lane LD, Buckey JC Jr, Cooke WH, Baisch FJ, Eckberg DL, and Blomqvist CG.** Human muscle sympathetic neural and haemodynamic responses to tilt following spaceflight. *J Physiol* 538: 331–340, 2002.
12. **Mano T.** Microneurography as a tool to investigate sympathetic nerve responses to environmental stress. *Aviakosm Ekolog Med* 31: 8–14, 1997.
13. **Michikami D, Kamiya A, Fu Q, Niimi Y, Iwase S, and Mano T.** Arm elevation enhances muscle sympathetic nerve activity during static exercise. *Environ Med* 44: 46–8, 2000.
14. **Mitchell JH and Victor RG.** Neural control of the cardiovascular system: insights from muscle sympathetic nerve recordings in humans. *Med Sci Sports Exerc* 28: S60–S69, 1996.
15. **Pagani M, Iellamo F, Lucini D, Cerchiello M, Castrucci F, Pizzinelli P, Porta A, and Malliani A.** Selective impairment of excitatory pressor responses after prolonged simulated microgravity in humans. *Auton Neurosci* 91: 85–95, 2001.
16. **Ray CA, Secher NH, and Mark AL.** Modulation of sympathetic nerve activity during posthandgrip muscle ischemia in humans. *Am J Physiol Heart Circ Physiol* 266: H79–H83, 1994.
17. **Riley DA, Bain JL, Thompson JL, Fitts RH, Widrick JJ, Trappe SW, Trappe TA, and Costill DL.** Thin filament diversity and physiological properties of fast and slow fiber types in astronaut leg muscles. *J Appl Physiol* 92: 817–825, 2002.
18. **Seals DR.** Influence of force on muscle and skin sympathetic nerve activity during sustained isometric contractions in humans. *J Physiol* 462: 147–159, 1993.
19. **Seals DR and Enoka RM.** Sympathetic activation is associated with increases in EMG during fatiguing exercise. *J Appl Physiol* 66: 88–95, 1989.
20. **Seals DR and Victor RG.** Regulation of muscle sympathetic nerve activity during exercise in humans. *Exerc Sport Sci Rev* 19: 313–349, 1991.
21. **Spaak J, Sundblad P, and Linnarsson D.** Impaired pressor response after spaceflight and bed rest: evidence for cardiovascular dysfunction. *Eur J Appl Physiol* 85: 49–55, 2001.
22. **Sterns DA, Ettinger SM, Gray KS, Whisler SK, Mosher TJ, Smith MB, and Sinoway LI.** Skeletal muscle metaboreceptor exercise responses are attenuated in heart failure. *Circulation* 84: 2034–2039, 1991.
23. **Ten Harkel AD, Beck L, and Karemaker JM.** Influence of posture and prolonged head-down tilt on cardiovascular reflexes. *Acta Physiol Scand Suppl* 604: 77–87, 1992.
24. **Wallin BG and Fagius J.** Peripheral sympathetic neural activity in conscious humans. *Annu Rev Physiol* 50: 565–576, 1988.
25. **Wautenpaugh DE and Hargens AR.** The cardiovascular system in microgravity, In: *Handbook of Physiology. Environmental Physiology. The Gravitational Environment.* Bethesda, MD: Am. Physiol. Soc., 1996, sect. 4, vol. I, chapt. 29, p. 631–674.
26. **Wesseling KH, Jansen JRC, Settels JJ, and Schreuder JJ.** Computation of aortic flow from pressure in humans using a nonlinear, three-element model. *J Appl Physiol* 74: 2566–2573, 1993.

PAPER *Special Section on Wide Band Systems*

Combined Iterative Demapping and Decoding for Coded MBOK DS-UWB Systems

Kenichi TAKIZAWA[†a)], *Member and* Ryuji KOHNO[†], *Fellow*

SUMMARY This paper presents a novel decoding strategy called *combined iterative demapping/decoding* (CIDD), for coded M-ary biorthogonal keying-based direct sequence ultra-wideband (MBOK DS-UWB) systems. A coded MBOK DS-UWB system consists of a convolutional encoder, an interleaver, and an MBOK DS-UWB pulse mapper. CIDD improves the error rate performance of MBOK DS-UWB systems by applying the turbo principle to the demapping and decoding processes at the receiver side. To develop the CIDD, a soft-in/soft-out MBOK demapping algorithm, based on the max-log-MAP algorithm, was derived. Simulation results showed that using CIDD siginificantly improved the error rate performance of both static and multipath fading channels. It was also shown that the computational complexity of CIDD is comparable to that of the Viterbi decoding used in $[133, 171]_8$ conventional convolutional coding.

key words: *ultra wideband, iterative decoding, M-ary biorthogonal keying(MBOK), multipath fading channels*

1. Introduction

Ultra-wideband (UWB) systems spread data over a very large band-width (at least 500 MHz according to FCC regulations) using low power spectral density. These UWB systems are of considerable interest, especially for the use in wireless personal area networks (WPAN) [1], because of their potential to enable high speed data transmission of up to 1 Gbps with low power consumption.

At present, UWB systems fall into three categories: impulse [2], [3], direct-sequence (DS) [4] and multiband [5], [6]. DS-UWB systems are capable of achieving a high data rate of up to 1 Gbps with relatively low complexity and have therefore been submitted to the IEEE802.15.3a Standards Commitee as a PHY proposal. One of these systems is M-ary biorthogonal keying-based DS-UWB, called MBOK DS-UWB [4]. However, the error rate performance of DS-UWB systems, including the MBOK DS-UWB, is seriously degraded by interpulse or intersymbol interference generated by multipath fading. There is therefore a need for low complexity methods that can compensate for this degradation.

A straightforward and effective solution to the problem is to use channel coding. Several channel coding strategies have been proposed for UWB systems [7], [8]. However, these methods require high computational complexity for the decoding process. In current proposal of the MBOK DS-UWB systems [4], the $[133, 171]_8$ conventional convolutional code is used to lower the decoding complexity. However, since the coding gain obtained from the convolutional code is insufficient to compensate for the degradation, an additional equalizer is required, increasing the cost of implementation.

In this paper, a novel demapping and decoding strategy, called combined iterative demapping and decoding (CIDD), is proposed for coded MBOK DS-UWB systems. The strategy is based on the turbo principle [9].

The paper is organized as follows. In the following section, a model of a coded MBOK DS-UWB system is illustrated. Section 3 includes an overview of the CIDD strategy and show how the soft-input/soft-output (SISO) MBOK pulse demapping algorithm based on the max-log-MAP algorithm is derived. An approximate upper bound is also derived for the bit error probability of an MBOK DS-UWB system using CIDD for the static channels. Section 4 describes the results of a simulation to evaluate the performance of the proposed system and the upper bounds derived, and Sect. 5 includes a discussion of the computational complexity. The paper is summarized in Sect. 6.

2. Coded MBOK DS-UWB Systems

2.1 Overview

Figure 1 shows a block diagram of a coded MBOK DS-UWB transmitter. The transmitter consists of a convolutional encoder, a bit-wise interleaver and an MBOK pulse mapper. In this paper, we focus on convolutional code used for the channel coding. The convolutional encoder encodes information-bit sequences $u(k)$ into codewords $c(n)$ of length N. The coding rate is denoted as R_c. After interleaving, interleaved codewords $c'(n)$ are mapped into a train of UWB pulse signals, denoted as $x(t)$, at the MBOK pulse mapper.

Figure 2 illustrates the function of the MBOK pulse mapper. An MBOK maps $K = \log_2 M$ bits into the selected biorthogonal code of length L_c from an assigned code set C in which one half of the codes are the complementary codes

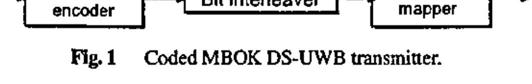

Fig. 1 Coded MBOK DS-UWB transmitter.

Manuscript received February 22, 2004.
Manuscript revised May 17, 2004.
Final manuscript received June 21, 2004.

[†]The authors are with UWB Technology Institute, National Institute of Information and Communications Technology, Yokosuka-shi, 239-0847 Japan.
a) E-mail: takizawa@nict.go.jp

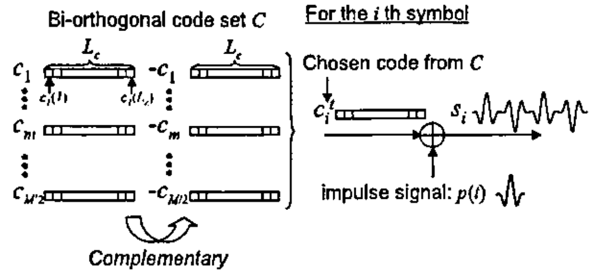

Fig. 2 MBOK DS-UWB pulse mapper.

of the other half. The MBOK pulse mapper maps the i th block of K bits, given by $c'((i-1)K+1), \cdots, c'(iK)$, into the selected code c_i^t. This code c_i^t is modulated by an impulse signal $p(t)$ as

$$s_i(t) = \sum_{j=1}^{L_c} c_i^t(j) \cdot p(t - j \cdot T_c) \tag{1}$$

where T_c denotes the chip time duration. The impulse signal $p(t)$ has a time duration of T_p and energy of $E_p = \int_0^{T_p} |p(t)|^2 dt$. The transmitted signal $x(t)$ is expressed by

$$x(t) = \sum_{i=1}^{N/K} s_i(t - i \cdot T_s) \tag{2}$$

where T_s denotes the symbol time duration, which is equal to $T_c \cdot L_c$.

In this paper, both static and multipath fading channels are considered. In a multipath fading channel, the impulse response is given by

$$h = \sum_{l=0}^{L-1} h_l \delta(t - \tau_l) \tag{3}$$

where L denotes the number of multipaths, and h_l and τ_l are the path gain and delay time, respectively, of the lth path. In this model, the received signals $r(t)$ are given by

$$r(t) = \sum_{l=0}^{L-1} h_l \cdot x(t - \tau_l) + n(t) \tag{4}$$

where $n(t)$ is Gaussian noise with a zero mean and variance σ^2.

Figure 3 shows a receiver architecture presented previously [4]. In this receiver, a received signal $r(t)$ is first correlated with an impuse signal $p(t)$. For the n_c th chip, the chip correlator outputs

$$z(n_c) = \int_0^{T_p} r(t + n_c \cdot T_p + \tau_d) p(t) dt \tag{5}$$

where τ_d stands for a timing jitter component. When perfect coherent detection is available, the term τ_d can be neglected. The correlator outputs on the pulse chip $z(n_c)$ are correlated with the $c_m \in C$. The code correlator output is given by

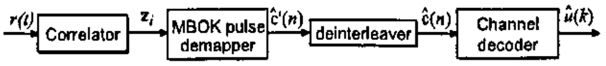

Fig. 3 Usual MBOK DS-UWB receiver architecture of transmitter shown in Fig. 1.

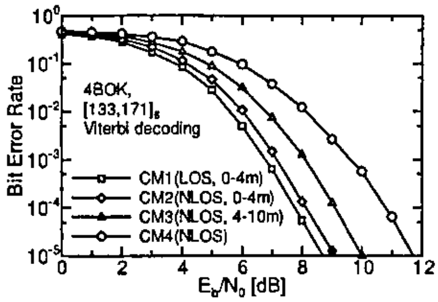

Fig. 4 Bit error rate performance based on propoed system [4] (16-finger rake combining, $[133, 171]_8$ convolutional code, hard decision Viterbi decoding, block interleaver with 360-bit length, 4BOK pulse mapping, and no equalizer).

$$z_{i,m} = \sum_{j=1}^{L_c} z(j + (i-1) \cdot L_c) c_m(j) \tag{6}$$

In multipath fading environments, rake combining is used to capture the energies of dispersive paths [10]. When rake combining is used after pulse correlation, the correlator outputs are rewritten as

$$z_{i,m} = \sum_{f=1}^{N_f} \alpha_f \sum_{j=1}^{L_c} z_i(j - \tau_f + (i-1) \cdot L_c) c_m(j) dt \tag{7}$$

where N_f denotes the number of rake fingers, and α_f and τ_f denotes the weight and time delay for the fth rake finger, respectively. The corelator outputs for the i th symbol are denoted as

$$\mathbf{z}_i = \{z_{i,1}, \ldots, z_{i,m}, \ldots, z_{i,M/2}\}. \tag{8}$$

In the usual architecture shown in Fig. 3, the correlator outputs $\mathbf{z}_i$ are fed to a MBOK demapper to obtain codewords $\hat{c}'(n)$. After deinterleaving, the codewords $\hat{c}(n)$ are decoded using a Viterbi decoder to obtain a decision $\hat{u}(k)$.

2.2 What is the Problem?

The receiver shown in Fig. 3 is greately influenced by multipath fading conditions. In Fig. 4, simulation results demonstrate this influence, where E_b/N_0 stands for the signal-to-noise ratio per bit. The four-channel model used (CM1, CM2, CM3, and CM4) is the model provided by IEEE 802.15.3a [11]. The best and worst performances were observed in CM1 and CM4, respectively. Note that the difference in the required E_b/N_0 between CM1 and CM4 at a bit-error probability of 10^{-5} was more than 3 dB. This result indicates that channel conditions have a significant influence on error-rate performance in coded MBOK DS-UWB systems. In this paper, we attempt to overcome this problem by using a demapping and decoding strategy at the receiver side.

3. Combined Iterative Demapping and Decoding

In this section, the proposed demapping and decoding strategy called combined iterative demapping and decoding (CIDD) is described.

3.1 Overview of CIDD

The CIDD applies the turbo principle [9] to the demapping and decoding of coded MBOK DS-UWB systems. By passing soft information via interleaving/deinterleaving between the soft-input /soft-output (SISO) demapper and decoder iteratively, the CIDD gradually improves the error rate performance.

A block diagram of an MBOK DS-UWB receiver with the CIDD is shown in Fig. 5. The main difference between this receiver and the usual type is the presence of a feedback structure with an interleaver. In this receiver, correlator outputs $\mathbf{z}_i$ are fed to a SISO MBOK demapper to obtain soft information on each bit of $c'(n)$. This soft information, which is based on the log likelihood ratio, $L(c'(n))$ is defined as

$$L(c'(n)) = \log \frac{P(c'(n) = 1|\mathbf{z}_i)}{P(c'(n) = 0|\mathbf{z}_i)} \tag{9}$$

The $L(c'(n))$ is fed into the SISO channel decoder as a priori information $L_a(c(n))$ after subtracting and deinterleaving. This decoder outputs soft information on both information bits $u(k)$ and codewords $c(n)$. The output $L(u(k))$ is used to make hard decisions $\hat{u}(k)$, and the other $L(c(n))$ is fed back into the SISO MBOK pulse demapper as a priori information $L_a(c'(n))$ after subtracting and interleaving.

Various SISO decoding algorithm have been developed for convolutional decoding [12]. In this paper, the max-log-MAP algorithm is used as the SISO decoding algorithm in the convolutional decoder because of its lower complexity compared to other algorithms. However, it is necessary to derive a SISO demapping algorithm for the MBOK pulse demapper to carry out CIDD.

3.2 SISO MBOK Pulse Demapping Algorithm

In this section, a SISO demapping algorithm based on the max-log-MAP algorithm for an MBOK pulse demapper is derived.

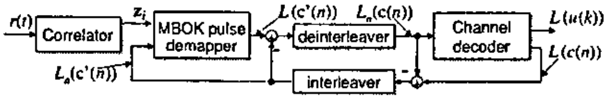

Fig. 5 Configuration of receiver with CIDD.

After obtaining the correlator outputs $\mathbf{z}_i$, the log-likelihood ratio $L(c'(n))$ is given by

$$\begin{aligned} L(c'(n)) &= \log \frac{P(c'(n) = 1|\mathbf{z}_i)}{P(c'(n) = 0|\mathbf{z}_i)} \\ &= \log \frac{\sum_{c'(n)=1, c_m \in C} P(c_m|\mathbf{z}_i)}{\sum_{c'(n)=0, c_m \in C} P(c_m|\mathbf{z}_i)} \end{aligned} \tag{10}$$

where $i = \lceil n/K \rceil$. By applying the Bayesian theorem to the above equation, we obtain

$$L(c'(n)) = \log \frac{\sum_{c'(n)=1, c_m \in C} P(\mathbf{z}_i|c_m) \cdot P(c_m)}{\sum_{c'(n)=0, c_m \in C} P(\mathbf{z}_i|c_m) \cdot P(c_m)} \tag{11}$$

Next, the max-log-MAP algorithm is applied to Eq. (11) to reduce computational complexity.

$$\begin{aligned} L(c'(n)) &= \log \sum_{c'(n)=1, c_m \in C} P(\mathbf{z}_i|c_m) \cdot P(c_m) \\ &\quad - \log \sum_{c'(n)=0, c_m \in C} P(\mathbf{z}_i|c_m) \cdot P(c_m) \\ &\approx \log \max_{c'(n)=1, c_m \in C} [P(\mathbf{z}_i|c_m) \cdot P(c_m)] \\ &\quad - \log \max_{c'(n)=0, c_m \in C} [P(\mathbf{z}_i|c_m) \cdot P(c_m)] \\ &= \max_{c'(n)=1, c_m \in C} [\log P(\mathbf{z}_i|c_m) + \log P(c_m)] \\ &\quad - \max_{c'(n)=0, c_m \in C} [\log P(\mathbf{z}_i|c_m) + \log P(c_m)] \end{aligned} \tag{12}$$

It is found from Eq. (12) that the $L(c'(n))$ can be obtained from the $\log P(\mathbf{z}_i|c_m)$ and $\log P(c_m)$, which stand for the logarithms of the conditional probability and a priori probability, respectively.

First, the term $\log P(\mathbf{z}_i|c_m)$ is considered. Assuming static AWGN channels and no timing jitters $\tau_d = 0$, the $\log P(\mathbf{z}_i|c_m)$ is rewritten as

$$\log P(\mathbf{z}_i|c_m) = \frac{z_{i,m}}{\sigma_z^2} + A_c \tag{13}$$

where the A_c denotes a constant value for all the c_m, and σ_z^2 stands for the noise variance in the correlator outputs. In practical applications, σ_z^2 is replaced by an estimated value $\hat{\sigma}_z^2$ or a constant value.

The other term $\log P(c_m)$ can be derived from the a priori information $L_a(c'(n))$ fed back from the SISO channel decoder. Let $\mathbf{b}'_m = \{b'_m(1), \ldots, b'_m(K)\}$ denote the K-bit sequence to be mapped to the c_m. Based on that $P(c_m)$ is equal to $P(\mathbf{b}'_m)$, and $\log P(c_m)$ for the i th symbol can be represented as

$$\begin{aligned} \log P(c_m) &= \log P(\mathbf{b}'_m) \\ &= \sum_{n=1+(i-1)K}^{i \cdot K} \log P(c'(n) = b'_m(n_k)) \\ &= \sum_{n=1+(i-1)K}^{i \cdot K} L_a(c'(n)) \cdot b'_m(n_k) + A_c \end{aligned} \tag{14}$$

where the index n_k denotes a relative index defined by

$$n_k = n - (i-1)K, \tag{15}$$

and the A_c is a common term between all the c_m. Details of the derivation of Eq. (14) are in Appendix.

Substituting Eq. (14) and Eq. (13) into Eq. (12), we obtain

$$L(c'(n)) \approx \max_{c'(n)=1, c_m \in C}\left(\frac{z_{i,m}}{\sigma_z^2} + \sum_{n=1+(i-1)\cdot K}^{i\cdot K} L_a(c'(n)) \cdot b'_m(n_k)\right) - \max_{c'(n)=0, c_m \in C}\left(\frac{z_{i,m}}{\sigma_z^2} + \sum_{n=1+(i-1)\cdot K}^{i\cdot K} L_a(c'(n)) \cdot b'_m(n_k)\right) \tag{16}$$

Note that the SISO demapping algorithm thus derived for an MBOK demapper does not need to perform complex operations, such as logarithm or exponential functions.

3.3 Performance Bounds for Static Channels

An upper bound on the bit error probability after CIDD processing is useful in analyzing its performance. However, it is difficult to derive an accurate bound after a certain number of iterations. Therefore, in this subsection, we derive a union bound based on soft maximum-likelihood (ML) decoding for an equivalent block code, as shown in Fig. 6. As noted in [13], this union bound becomes closer to the error rate performance of the CIDD after sufficient iterations.

The union bound on the bit error probability for a linear block code is given by [13]

$$P_b \leq \frac{1}{2}\sum_{w=1}\sum_{d=d_m}\frac{w}{N \cdot R_c}A_{w,d}P_d \tag{17}$$

where $A_{w,d}$ denotes the number of codewords with a Hamming distance of w between the input sequences and a Euclidean distance of d between the output signal and the correct one. In Eq. (17), d_m denotes the minimum distance of d, and P_d stands for the pairwise error probability corresponding to d. The Euclidean distance d is defined as

$$d = \int_0^{T_s \cdot N/K} \left|x(t) - \hat{x}(t)\right|^2 dt \tag{18}$$

where $x(t)$ is a correct signal and $\hat{x}(t)$ is an erroneous one. In this derivation, the correct signal is set as the signal generated by all zero codeword.

For a static channel, the pairwise error probability P_d is given by

$$P_d = \frac{1}{2}\mathrm{erfc}\left(\sqrt{\frac{d}{4\sigma_z^2}}\right) \tag{19}$$

Fig. 6 Equivalent block code for obtaining upper bounds for static channels.

where erfc(x) means the complementary error function given by

$$\mathrm{erfc}(x) = \frac{2}{\sqrt{\pi}}\int_x^{\infty} e^{-y^2}dy \tag{20}$$

Next, the derivation of the $A_{w,d}$ is considered. Unfortunately, counting the $A_{w,d}$ for a combination of convolutional coding and MBOK mapping imposes a heavy load because there may be up to 2^N codewords. However, the individual weights (or distance) spectra, given by $A^{\mathrm{C}}_{w,h}$ for convolutional coding and $A^{\mathrm{MBOK}}_{h,d}$ for MBOK pulse mapping, are tractable. The $A^{\mathrm{C}}_{w,h}$ can be obtained theoretically [14], and the $A^{\mathrm{MBOK}}_{h,d}$ can be enumerated by a computer search within a short period. By assuming the use of uniform random interleving [13], the whole codeword spectra $A_{w,d}$ can be approximately written as

$$A_{w,d} \approx \sum_h \frac{A^{\mathrm{C}}_{w,h} \cdot A^{\mathrm{MBOK}}_{h,d}}{\binom{N}{h}} \tag{21}$$

The uniform random interleaver converts a codeword with weight h into a codeword with the same weight in $\frac{1}{\binom{N}{h}}$.

The upper bound on the bit error probability can then be obtained by substituting the derived P_d and $A_{w,d}$ into Eq. (17).

4. Performance Evaluation

4.1 Simulation Results for Static Channels

First, the simulation results for the static channels are presented to demonstrate the performance of the CIDD. The simulation parameters are listed in Table 1. The use of

Table 1 Simulation parameters for static channels.

MBOK pulse mapping	4BOK or 8BOK
Convolutional code	$[5, 7]_8$ or $[15, 17]_8$
Coding rate	$R_c = 1/2$
Channel decoding algorithm	max-log-MAP
Interleaver	uniform random interleaver
Interleaver size	$N = 360$ bits
Channel estimation	perfect on σ_z^2
Detection	coherent ($\tau_d = 0$)
Chip rate	1.368 GHz

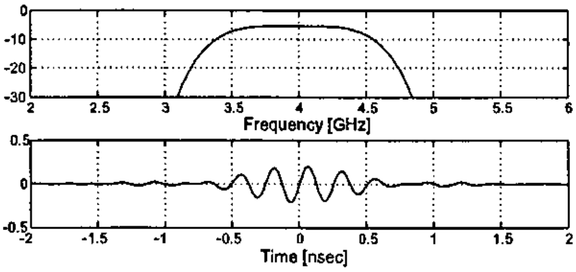

Fig. 7 Pulse shapes of root-raised cosine pulse signals in time and frequency domain.

Table 2 Ternary codes for MBOK DS-UWB systems.

$c_1 = \{-1\ \ 1\ \ -1\ \ -1\ \ 1\ \ -1\ \ -1\ \ 1\ \ -1\ \ 0\ \ -1\ \ 0\ \ -1\ \ -1\ \ 1\ \ 1\ \ 1\ \ -1\ \ 1\ \ 1\ \ 1\ \ -1\ \ -1\ \ -1\}$

$c_2 = \{-1\ \ -1\ \ 1\ \ 0\ \ 1\ \ 1\ \ 1\ \ -1\ \ -1\ \ 1\ \ -1\ \ 1\ \ 1\ \ -1\ \ 1\ \ 0\ \ 1\ \ -1\ \ -1\ \ -1\ \ 1\ \ -1\ \ -1\ \ -1\}$

$c_3 = \{-1\ \ 1\ \ -1\ \ 1\ \ -1\ \ -1\ \ 0\ \ 1\ \ -1\ \ -1\ \ -1\ \ 1\ \ -1\ \ -1\ \ 1\ \ 0\ \ -1\ \ -1\ \ -1\ \ -1\ \ 1\ \ 1\ \ 1\ \ 1\}$

$c_4 = \{-1\ \ -1\ \ 1\ \ 1\ \ 1\ \ -1\ \ -1\ \ -1\ \ -1\ \ -1\ \ -1\ \ 0\ \ -1\ \ 1\ \ -1\ \ 1\ \ -1\ \ 1\ \ 1\ \ -1\ \ 1\ \ 1\ \ -1\ \ 0\}$

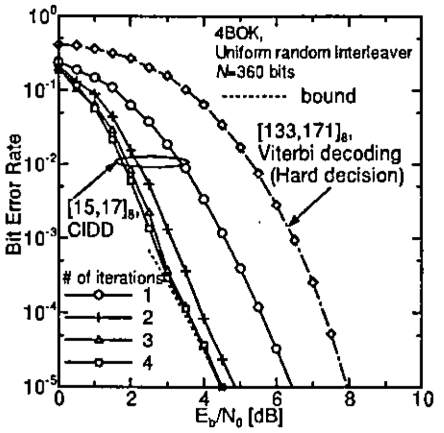

Fig. 8 Bit error rate performance for static (AWGN) channel.

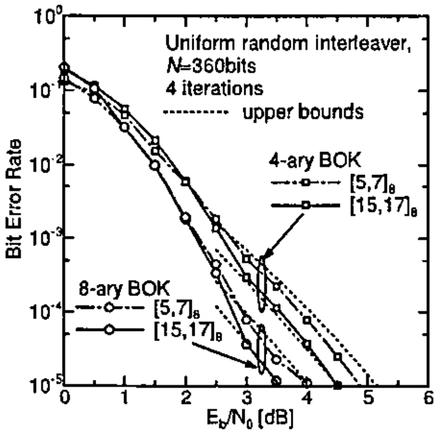

Fig. 9 Bit error rate performance for 4 and 8BOK and $[5,7]_8$ and $[15,17]_8$ convolutional codes.

a short interleaver is to show that the CIDD works well, even for short-length packets. The pulse signal used $p(t)$ and ternary spreading codes $c_m(m = 1, \cdots, 4)$ are shown in Fig. 7 and Table 2, respectively. The bandwidth of the pulse signal is about 1.5 GHz at −10 dB down from the peak level. The pulse signal, spreading codes, and chip rate were the same as those used in [4]. The convolutional codes, $[5,7]_8$ and $[15,17]_8$, are the optimum codes from the viewpoint of maximizing the minimum distance of the equivalent block code shown in Sect. 3.3.

Simulation results are shown in Fig. 8, where the bit error rate performance is plotted after each iteration of the $[15,17]_8$ coded 4BOK system. The upper bound on the bit error probability is also plotted. These results show that the CIDD significantly improved the error rate performance through iterative processing significantly. The gain derived from the use of CIDD is more than 3.5 dB with a bit error rate of 10^{-5} in comparison with the use of a combination of $[133,171]_8$ coding and Viterbi decoding. In addition, the derived bound fit the simulation results well after three iterations with a bit error rate of less than 10^{-4}.

Next, the simulation results for the 4 and 8BOK and the $[5,7]_8$ and $[15,17]_8$ convolutional codes are shown in Fig. 9. In this figure, the upper bounds on the bit error rate are also plotted for comparison. As the figure shows, the required E_b/N_0 at 10^{-5} was reduced by the increase in M or memory length ν. As a result, a gain of about 0.5 dB can be ontained by replacing the $[5,7]_8$ code with the $[15,17]_8$ code, and a 1 dB gain can be obtained by replacing the 4BOK ($M = 4$) with the 8BOK ($M = 8$). These improvements result from an increase in the minimum distance d_m.

4.2 Interleaving

In applying the turbo principle, the type of interleaver used has considerable influence on performance. In this section, the most suitable type of interleaver for applying CIDD to MBOK DS-UWB systems is discussed.

Various kinds of interleavers have been invented, e.g., block, convolutional, code-matched [15], and S-random [16]. The following points should be considered in selecting a suitable interleaver. It should:

- accept codewords of various lengths.
- have a structure that is easy to implement.
- improve the error rate performance.
- be capable of breaking the correlation between the bits contained in an MBOK symbol.

Taking the first and second points into account rules out the use of a code-matched interleaver. Interleavers based on statistics, such as an S-random interleaver, are also unsuitable because they do not satisfy the second point. In addition, block interleavers present difficulties because they may fail to break certain low-weight input patterns, as previously noted [12]. However, cyclic shift interleavers [12], which include convolutional interleavers, satisfy all of the requirements and are therefore suitable for applying CIDD to MBOK DS-UWB systems.

The results of a simulation to assess the performance of the cyclic shift interleaver are shown in Fig. 10. For a comparison, the results of using block, uniform random in-

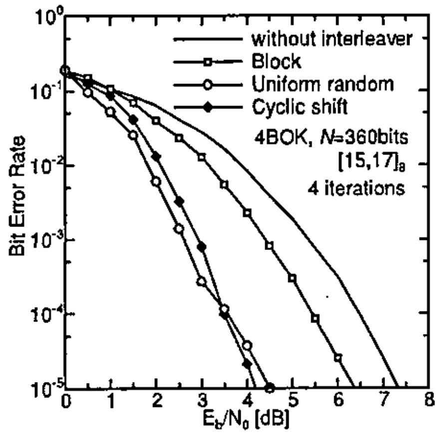

Fig. 10 Bit error rate performance after four iterations using different interleavers.

terleavers, and no interleaver, are also shown. In the simulation, the block and cyclic shift interleavers performed interleaving using a 6 × 60 matrix. In cyclic shift interleaving, the value of the bit shifts in each row B was set at six. As the results show, the cyclic shift interleaver achieved a bit error rate of 10^{-5} with the lowest E_b/N_0. At around 10^{-4}, the performance of the cyclic shift interleaver exceeded that of the uniform random interleaver. This is because the uniform random interleaver may generate an output pattern that is the same as the input pattern.

4.3 Multipath Fading Channels

In this section, the simulation results for multipath fading channels are discussed. The channel model used is the four-channel model provided by the IEEE802.15.3a. The channels are CM1, CM2, CM3, and CM4 and their characteristics are listed in Table 3. In this table, $NP_{10\,dB}$ is the number of paths within 10 dB of the strongest path, and $NP_{85\%}$ represents the number of paths containing 85% of the energy. These models assume that the channel impulse response is constant during transmission of a packet if it is shorter than 200 μsec. The system parameters are shown in Table 4. In multipath fading channels, rake combining can be used to capture dispersive path energies. In the simulations, a selection rake (s-rake) combining [10] was used in which the largest F paths were coherently combined. In the relation to the use of s-rake combining, we assumed that the time shifts τ_f and weights α_f in Eq. (7) were estimated perfectly. The SISO MBOK demapping algorithm was not modified in any way, even though the channel models were replaced by multipath fading channels and rake combining was used.

Table 3 Characteristics of channel model provided by IEEE802.15.TG3a based on sampling time 167 psec [11].

	CM1	CM2	CM3	CM4
Channel model	LOS	NLOS	NLOS	NLOS
Mean excess delay [nsec]	4.9	9.4	13.8	26.8
RMS delay [nsec]	5	8	14	26
$NP_{10\,dB}$	13.3	18.2	25.3	41.4
NP(85%)	21.4	37.2	62.7	122.8
Channel energy mean [dB]	-0.5	0.1	0.2	0.1
Channel energy STD [dB]	2.9	3.3	3.4	3.2

Table 4 Simulation parameters for multipath fading channels.

MBOK pulse mapping	4BOK
Convolutional code	$[15,17]_8$
Coding rate	$R_c = 1/2$
Channel decoding algorithm	max-log-MAP
Interleaver	cyclic shift interleaver ($B = 6$)
Interleaver size	$N = 360$ bits
Channel estimation	perfect on σ_z^2, α_f and τ_f
Rake combining	16-finger s-rake
Detection	coherent ($\tau_d = 0$)
Chip rate	1.368 GHz
Equalizer	Not used

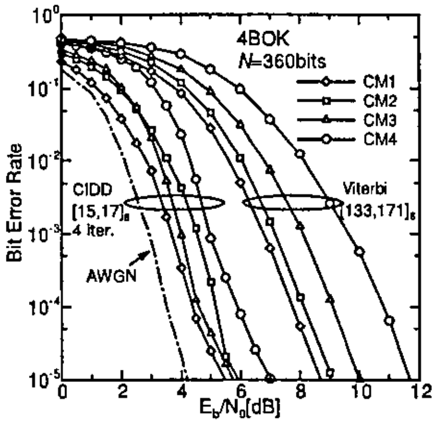

Fig. 11 Bit error rate performances for multipath fading channels.

The simulation results are shown in Fig. 11. In this figure, the results for the $[133,171]_8$ convolutional coded 4BOK system using Viterbi decoding are also shown for comparison. As the results show, the use of CIDD clearly provides better performance than Viterbi decoding for all of the channels. With the CIDD, the results for CM3 were superior to those for CM2. This is because the SISO MBOK demapping algorithm that was used is not optimum for multipath fading channels and receivers using rake combining. However, the results show that the simple demapping algorithm derived in Sect. 3.2 can significantly improve error rate performance. In addition, the difference in the E_b/N_0 required to satisfy the 10^{-5} between CM1 and CM4 was less than 1.5 dB. This demonstrates that an MBOK DS-UWB with CIDD can provide stable performance in various multipath fading environments. CIDD improves performance by means of iterative processing, which updates the likelihood information for MBOK symbols using a priori information from the SISO decoder, as shown in Eq. (16). Figure 12 shows the transition in the bit error rate performance for CM3, demonstrating the improvements generated by the iterative process. In other words, this iterative process can be viewed as playing a similar role to a decision-feedback equalizer. CIDD produces these improvements in multipath fading channels without requiring an equalizer.

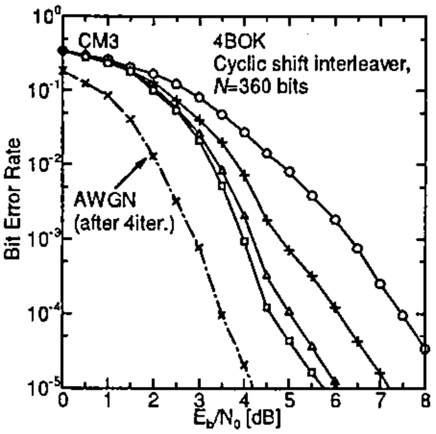

Fig. 12 Bit error rate performance in CM3 channel.

5. Computational Complexity

In this section, the computational complexity of CIDD is estimated using the *equivalent additions* method proposed by Wu [17]. This method estimates the total complexity of signal processing by translating the complexity of each operation into ADD operations. In Table 5, the relative complexities of ADD, SUB, MUL, and MAX are shown.

Table 5 Equivalent addition for some operations [17].

Operations	ADD	SUB	MUL	MAX
Computational complexity	1	1	1	2

First, the complexity of the SISO MBOK pulse demapping algorithm is estimated. The required computation number per symbol for each operation is shown in Table 6. The total complexity per codeword of length N is given by

Table 6 Number of times ADD, SUB, MUL, and MAX opertions occur per symbol in derived SISO MBOK demapper.

Type	ADD	SUB	MUL	MAX
# of times	$K \cdot M$	K	$M \cdot (K+1)$	$\left(\frac{M}{2}-1\right)K$

$$C_p = \frac{N}{K}\{4K(M-1)+2M\} \tag{22}$$

With 4BOK and 8BOK, the complexity is 5760 and 12000, respectively, with an interleaver size of $N = 360$.

The complexity of the SISO convolutional decoding algorithm based on the max-log-MAP algorithm has also been derived [17], and is given by

$$C_c = (34 \cdot 2^{\nu} - 9) \cdot \frac{N}{2} \tag{23}$$

In the case of $N = 360$, the complexity reaches 22860 and 47340 for $\nu = 2$ and 3 convolutional codes, respectively. Clearly, the complexity of the convolutional decoder is the largest factor in the total complexity. After N_i iterations, the total complexity C_{total} is given by

$$C_{\text{total}} = (C_p + C_c) \cdot N_i \tag{24}$$

Note that we did not consider the computational complexity of interleaving and deinterleaving when estimating the total computational complexity. This is because most of the interleavers applicable to CIDD do not require any computational operations even though access to a memory is required.

Figure 13 shows the bit error rate performance versus computational complexity for 4 and 8BOK DS-UWB systems with CIDD. For comparison, the simulation results are also shown for $[133, 171]_8$ coded MBOK DS-UWB system using Viterbi decoding. The complexity of the Viterbi decoding is given by [17]

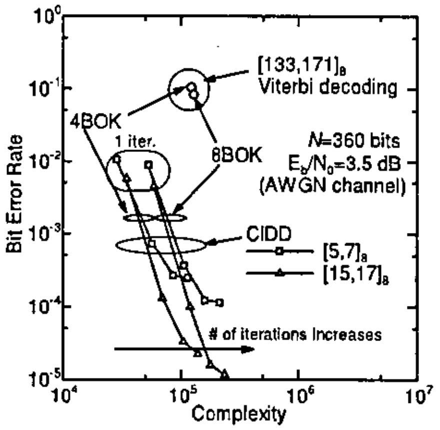

Fig. 13 Bit error rate performance versus computational complexity for static channels.

$$C_v = C_p + (10 \cdot 2^{\nu} + 6) \cdot \frac{N}{2} \tag{25}$$

As the results for 4 and 8BOK show, comparing with Viterbi decoding, CIDD provides better performance with almost the same complexity.

Turbo coding, which is parallel concatenated convolutional coding, is an effective and popular coding method [12]. However, its decoding complexity may be larger than that of CIDD with the same memory length ν because a turbo decoder needs two constituent SISO convolutional decoders. The computational complexity of the max-log MAP-based constituent decoder is given by $C_{ct} = (26 \cdot 2^{\nu} - 3) \cdot \frac{N}{2}$ [17]. The total complexity of turbo decoding after N_i iterations is given by

$$C_t = C_p + N_i \cdot 2C_{ct} \tag{26}$$

Table 7 compares turbo decoding with CIDD in terms of complexity and performance. In turbo coding, each $R_c = 1/2$ code is obtained by puncturing the original $R_c = 1/3$ turbo code.

As these results show, compared with a turbo-coded system, CIDD is a superior decoding strategy in terms of complexity and performance improvement.

Table 7 Comparison of turbo decoding and CIDD in terms of complexity and performance ($M = 4, N = 360$ and $R_c = 1/2$).

	$[5,7]_8$		$[15,17]_8$	
	complexity	BER	complexity	BER
Turbo	1.51×10^5	6.48×10^{-3}	3.01×10^5	5.07×10^{-3}
CIDD	1.14×10^5	2.44×10^{-4}	1.39×10^5	2.25×10^{-5}

6. Conclusions

This paper discussed the use of a combined iterative demapping and decoding (CIDD) approach to improve the error rate performance of MBOK DS-UWB systems [4]. A SISO MBOK pulse demapping algorithm based on a max-log MAP algorithm was derived to enable the turbo principle to be applied to the CIDD.

The results showed that by using iterative decoding, CIDD improved the error rate performance of static channels, and the derived bounds fit the simulation results after sufficient iterations. In addition, the simulation results suggest that cyclic shift interleavers are suitable for MBOK DS-UWB systems using CIDD. It was also shown that in multipath fading channels, CIDD acts like a decision-feedback equalizer, improving error rate performance through iterative decoding without requireing an additional equalizer.

Finally, the computational complexity of CIDD was estimated using the equivalent addition method. The results showed that the computational complexity of CIDD is almost the same as that of the Viterbi decoding of $[133, 171]_8$ conventional convolutional code.

References

[1] D. Porcino and W. Hirt, "Ultra-wideband radio technology: Potential and challenges ahead," IEEE Commun. Mag., vol.41, no.7, pp.66–74, July 2003.

[2] M.Z. Win and R.A. Scholtz, "Ultra-wide bandwidth time-hopping spread spectrum impulse radio for wireless multiple-access communications," IEEE Trans. Commun., vol.48, no.4, pp.679–689, April 2000.

[3] H. Zhang, R. Kohno, and K. Takizawa, "CRL-UWB consortium's optimized soft-spectrum UWB PHY proposal update for IEEE 802.15.3a," IEEE802.15-03/387r0, Sept. 2003.

[4] M. Welborn, "Xtreme-spectrum CFP presentation," IEEE802.15-03/153r5, May 2003.

[5] J. Foerster, V. Somayazulu, S. Roy, E. Green, K. Tinsley, C. Brabenac, D. Leeper, and M. Ho, "Intel CFP presentation for a UWB PHY," IEEE802.15-03/109r1, March 2003.

[6] A. Batra, J. Balakrishnan, and A. Dabak, "TI physical layer proposal," IEEE802.15-03/141r1, March 2003.

[7] A.R. Forouzan, M. Nahiri-Kenari, and J.A. Salehi, "Low-rate convolutionally encoded time-hopping spread spectrum multiple access systems," Proc. IEEE PIMRC'00, vol.2, pp.1555–1558, Sept. 2000.

[8] N. Yamamoto and T. Ohtsuki, "Adaptive internally turbo-coded ultra wideband-impulse radio (AITC-UWB-IR) systems," Proc. IEEE ICC'03, pp.3535–3539, May 2003.

[9] J. Hagenauer, "The turbo principle-tutorial introduction and state of the art," Proc. Int. Symp. on Turbo-Codes, pp.1–11, Brest, France, Sept. 1997.

[10] A. Rajeswaran, V.S. Somayazulu, and J.R. Foerster, "Rake performance for a pulse based UWB system in a realistic UWB indoor channel," Proc. IEEE ICC'03, vol.4, pp.2879–2883, 2003.

[11] J. Foerster, "Channel modeling sub-committee report final," IEEE P802.15-02/368r5-SG3a, Sept. 2002.

[12] B. Vucetic and J. Yuan, Turbo codes—Principles and applications, Kluwer Academic Publishers, 2000.

[13] S. Benedetto, D. Divsalar, G. Montorsi, and F. Pollara, "Serial concatenation of interleaved codes: Performance analysis, design and iterative decoding," IEEE Trans. Inf. Theory, vol.44, no.3, pp.909–926, 1998.

[14] J. Proakis, Digital communications, 4th ed., McGraw Hill, 2000.

[15] W. Feng, J. Yuan, and B. Vucetic, "A code matched interleaver design for turbo codes," Proc. IEEE PIMRC'99, pp.578–582, Sept. 1999.

[16] D. Divsalar and F. Pollara, "Turbo codes for PCS applications," Proc. IEEE ICC'95, pp.54–59, June 1995.

[17] P.H.-Y. Wu, "On the complexity of turbo decoding algorithms," Proc. IEEE VTC'00-Spring, vol.2, pp.1439–1443, May 2001.

Appendix: Derivation of Eq. (14)

The logarithm of the a priori probability $P(c_m)$ is given by

$$\begin{aligned}\log P(c_m) &= \log P(\mathbf{b}'_m) \\ &= \sum_{n=1+(i-1)K}^{i\cdot K} \log P(c'(n) = b'_m(n_k)) \qquad \text{(A$\cdot$ 1)}\end{aligned}$$

The a priori probability for $c'(n)$ is expressed as

$$\begin{aligned}P(c'(n) = 0) &= \frac{1}{1 + e^{L_a(c'(n))}} \qquad \text{(A$\cdot$ 2)} \\ P(c'(n) = 1) &= 1 - P(c'(n) = 0) \\ &= \frac{e^{L_a(c'(n))}}{1 + e^{L_a(c'(n))}} \qquad \text{(A$\cdot$ 3)}\end{aligned}$$

By taking the logarithm of the above equations,

$$\begin{aligned}\log P(c'(n) = 0) &= -\log(1 + e^{L_a(c'(n))}) \qquad \text{(A$\cdot$ 4)} \\ \log P(c'(n) = 1) &= L_a(c'(n)) - \log(1 + e^{L_a(c'(n))}) \\ &= L_a(c'(n)) - \log P(c'(n) = 0) \qquad \text{(A$\cdot$ 5)}\end{aligned}$$

By using this relation, Eq. (A· 1) can be rewritten as

$$\log P(c_m) = \sum_{b'_m(n_k)=1} L_a(c'(n)) - \sum_{n=1+(i-1)K}^{i\cdot K} \log P(c'(n) = 0) \qquad \text{(A$\cdot$ 6)}$$

If the latter term, which is a common term among the all c_m, is set at A_c, then we obtain

$$\log P(c_m) = \sum_{n=1+(i-1)K}^{i\cdot K} L_a(c'(n)) \cdot b'_m(n_k) - A_c \qquad \text{(A$\cdot$ 7)}$$

where we introduce

$$\sum_{b'_m(n_k)=1} L_a(c'(n)) = \sum_{n=1+(i-1)K}^{i\cdot K} L_a(c'(n)) \cdot b'_m(n_k) \qquad \text{(A$\cdot$ 8)}$$

into Eq. (A· 6). Equation (14) is thus derived.

Kenichi Takizawa received the B.E., M.S., and Dr.Eng. degrees in 1998, 2000, and 2003, respectively, from Niigata University. He is currently a resercher of the UWB Technology institute of National Institute of Information and Communications Technology (NICT). He is a member of IEEE.

Ryuji Kohno received the Ph.D. degree in electrical engineering from the University of Tokyo in 1984. Dr. Kohno is a Professor of the Division of Physics, Electrical and Computer Engineering, Graduate School of Engineering, Yokohama National University (YNU) since 1998. Since October 2002 he has been a president of COE for Creation of Future Social Infrastructure Based on Information Telecommunications Technology in YNU. He was a director of Advanced Telecommunications Laboratory of SONY CSL during 1998–2002 and currently a director of UWB Technology institute of National Institute of Information and Communications Technology (NICT). In his academic activities, he was elected as a member of the Board of Governors of IEEE Information Theory Society in 2000 and 2003. Moreover, he was an associate editor of the IEEE Transactions on Information Theory during 1995–1998. Currently he is an associate editor of the IEEE Transactions on Communications since 1994, and IEEE Transactions on Intelligent Transport Systems (ITS) since 1999. He was the Chairman of the IEEE Professional Group on Spread Spectrum Technology during 1995–1998 and that of Intelligent Transport System (ITS) during 1998–2000, and currently that on Software Defined Radio (SDR).